Numerical modelling of mode penetration in cylindrical geometries using M3D-C1

Mackenbach, R.J.J.

Award date:
2019

Numerical Modelling of Mode Penetration in Cylindrical Geometries using M3D-C1

R.J.J. Mackenbach
Under supervision of
N. Ferraro, J.H.E. Proll

A thesis presented for the degree
Master of Science

Science and Technology of Nuclear Fusion
Eindhoven University of Technology
The Netherlands
November 26, 2019

“If a machine is expected to be infallible, it cannot also be intelligent.”
Alan Turing

Contents

1 Introduction

The world, fusion energy, and this research

The earth is in dire need of help. As global energy consumption keeps increasing, so do greenhouse gas emissions. This in turn, through many feedback mechanisms [1, 2], raises the earth's average temperature and sea-levels. Since the energy-thirst of the human race is hard to quench, we must turn to renewable energy resources. Many options exist, but only few will be able to sustain the increasing need for energy in the long run. Fusion is one of those options.

There are many different concepts for a fusion energy power plant. The tokamak (a Russian acronym for "*toroidal chamber with magnetic coils*") is the leading candidate as of now (in terms of funding and technological readiness). This axisymmetric machine confines a plasma (an ionized gas) by making use of strong magnetic fields and large currents. The device is shaped like a doughnut, a necessity arising due to something called the Hopf-Poincaré theorem [3]. The plasma contains the fuel of our machine - the deuterium and tritium nuclei which will fuse into helium and produce energy. Using this configuration the tokamak tries to produce more energy than it consumes (quantified in Lawson's criterion [4]), a feat which ITER hopes to demonstrate. A sketch of a tokamak device can be seen in figure 1.1.

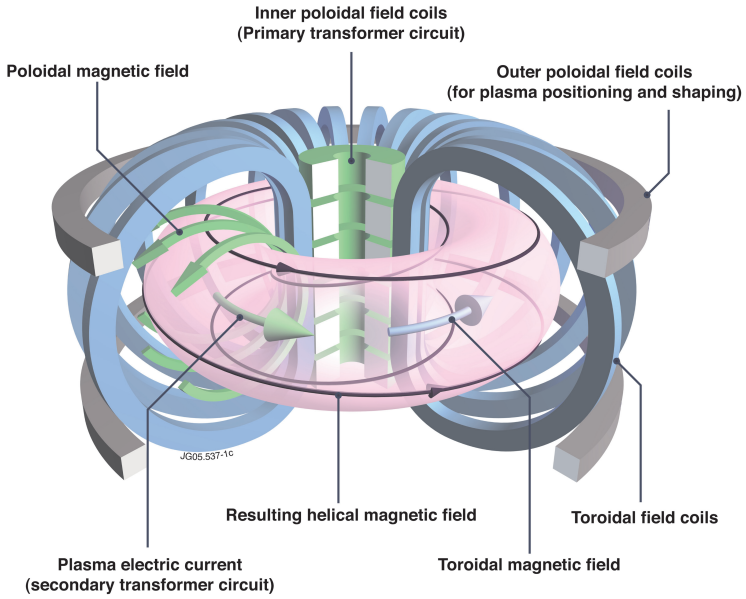

Figure 1.1: An illustration showing the essential workings of a tokamak. The toroidal field coils provide a strong magnetic field around the torus. The inner poloidal field coils provide a loop voltage, driving plasma currents. The plasma currents in turn give rise to a poloidal magnetic field, resulting in helical magnetic fields. Finally, some outer poloidal field coils are necessary for combating so-called hoop forces, and tire-tube forces. An important feature of the tokamak is that it is invariant under rotations (axisymmetric). This symmetry is ultimately responsible for a stable plasma configuration. Adapted from Eurofusion [5].

Tokamaks however, are not free of problems. These machines are plagued by many different complications, such as large heat fluxes and neutron activation of materials. An important complication of tokamaks we will be focusing on is a so-called disruption. During this cataclysmic event, a large amount of energy contained in the machine is released in a short amount of time. This can be seen in a number of different diagnostics: the plasma current suddenly drops, and the thermal energy stored in the plasma quickly falls as well. This can lead to a host of unwanted effects, such as runaway electrons, large heat fluxes, and induced structural forces on the machine. This possibly has awful consequences; structural integrity could be compromised, and essential components might break or melt due to the large heat fluxes. So, understanding how these disruptions might occur and be prevented is of vital importance for future operation of these machines.

These disruptions are often preceded by the growth of so-called magnetic islands [6]. Magnetic islands are regions of the plasma where the structure of the magnetic field is different than in the bulk of the plasma. Outside the magnetic island, field lines form nested surfaces around the magnetic axis (called flux surfaces). Within the island, the magnetic field lines form nested surfaces around a single magnetic field line which also resides in the island. This different structure has magnetic field lines which connects flux surfaces at different radial locations. Transport along these field lines is very fast, thus evening out temperature and density gradients. This is equivalent to having a region with highly enhanced transport. As islands grow, transport is enhanced further, which in turn degrades many of the important operational parameters of the tokamak (e.g. the plasma temperature, the plasma density, etc.). Understanding how islands can grow could help mitigate and reduce the risk of disruptions. For example, there are clear indications that magnetic island growth could be stifled due to plasma bulk flows [7]. The precise causal links between disruptions and these magnetic islands are still to be understood, but there is a clear interplay between the two.

One of the ways that magnetic islands can grow is via so called error-field penetration events, often also called mode-penetration events. Mode penetration refers to the sudden decrease of plasma bulk flow when an error-field (that is, a non-axisymmetric part of the magnetic field) exceeds some threshold value. Error-fields arise due to, for example, the discrete number of coils (ripple field), or induced currents in a resistive wall. The velocity decrease means that the plasma bulk flow velocity near the region where an island resides drops close to zero in a lab-frame of reference. As plasma velocity has a suppressing effect on island size, this sudden halt allows the island to grow, possibly leading to a disruption. There is plentiful experimental evidence for mode penetration events [8–11]. An experimental run showing growth in island width and halt in plasma velocity after an error-field penetration event is shown in figure 1.2. Here we see that when an error-field exceeds a critical value, magnetic islands suddenly grow and plasma bulk flow velocity is suppressed.

There are indications that mode-penetration events could be of importance to ITER, and future fusion power plants. Error fields in ITER are projected to be on the order of $\delta B/B \approx 10^{-4}$ which, as extrapolations from other machines have shown, could be sufficient to induce a mode-penetration event [12]. These error-fields could be

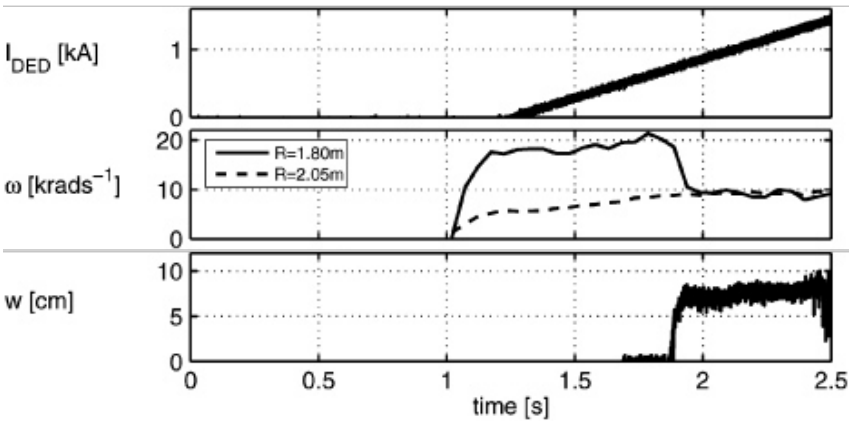

Figure 1.2: Graphs showing a few time-traces from TEXTOR shot #94444. From top to bottom one can see: DED current as a function of time, plasma rotation velocity at a specific radial coordinate as a function of time as measured via charge exchange spectroscopy, and island width as a function of time as measured via soft x-ray cameras. Error-fields are created by slowly increasing current through the Dynamic Ergodic Divertor (DED) in TEXTOR, a set of coils which are used to produce error-fields. The island width suddenly increases when the strength of the error field is increased beyond a critical threshold value, and correspondingly the plasma velocity drops. Adapted from Koslowski et al. [8].

reduced by introducing correcting coils and other measures, but it is a clear motivation to deepen and enhance understanding of this phenomenon.

Although some simulations have been done of this phenomenon [13, 14], these are often in highly simplified geometries and scenarios (e.g. slab geometries, neglecting external factors). It is the goal of this research to simulate such a mode-penetration event using M3D-C1 in a full cylindrical geometry, to gain understanding into the event and benchmark M3D-C1 in a non-linear regime. This is still a simplified model, but it is an important step towards a full toroidal simulation. Furthermore, the results are benchmarked against analytical theory and previous simulations [15, 16] to see how well they correspond. It is the eventual goal that mode-penetration events may be simulated in highly realistic (perhaps ITER relevant) scenarios, so that we may better understand its caveats.

It is important to note that M3D-C1 is an extended-MHD code, meaning that it does build on some set of assumptions (sufficient collisions between particles, electron mass negligible compared to the ion mass, etc.). One could question how much the physics behind mode-penetration would be altered if one would take an approach which build on less assumptions (for example, mode-penetration in a drift-kinetic model). This has been investigated and it is found that results are only slightly altered in these more realistic approaches [17, 18]. Thus, an MHD approach is justified. It is also favorable as these MHD codes are computationally less intensive than the more complex models.

We tackle the problem of simulating a mode-penetration event by divvying up the task into multiple sub-tasks. The first task consists of an investigation into the analytical theory, presented in section 2. This encapsulates the theory behind the MHD models used, and an investigation into the analytics of mode-penetration it-

self. For the theory behind mode-penetration we develop a novel heuristic model, meant to help us gain intuition in the physics behind mode-penetration. We also add a novel component into the model of mode-penetration which encapsulates an external effect which had not been accounted for before, namely the effect of external driving forces such as NBI-beams on mode-penetration. Finally, we also develop a novel set of equilibrium equations, meant to initialize the simulations.

After the excursion into theory, we investigate a previous simulation which is most similar to what we would like to achieve in M3D-C1, namely a case by Yu et al. [16]. This case is also makes use of a cylindrical geometry, and shows a mode-penetration event. To benchmark against this result, we build a set of simulations which are similar in M3D-C1. This is presented in section 3. In section 4, we investigate the results obtained by M3D-C1 to see if they show similar quantitative and qualitative results to the benchmark case. The differences of these results are discussed in section 5. Possible reasons for the discrepancies are highlighted, and some recommendations are made for future research. Finally, we present the main conclusions of the research in section 6.

2 Analytical theory

In this section, the analytical theory behind this thesis is elaborated. This consists of three different parts. Firstly, the two fluid model is derived which is employed by M3D-C1. Secondly, the theory behind mode penetration is elaborated to find scaling laws and relevant regions in parameter space. It is also expanded upon by adding novel components. Finally, a novel set of resistive viscous equations are derived, describing plasmas which are at equilibrium in a cylindrical geometry.

2.1 The two fluid model

It is important to understand the underlying physics on which M3D-C1 is built to understand its caveats and limitations. To do so, we derive the so-called two-fluid model (which M3D-C1 employs). We combine arguments from Freidberg, Braginskii, and Shkarofsky to make a comprehensive overview of the two-fluid model [19–21]. Although we will run M3D-C1 in a single-fluid mode, the deviations from the two-fluid model are only small. The two-fluid model will also be used to derive the so-called layer equations in the section on mode-penetration.

Distribution function and its moments

We suppose that there are enough particles in the system that a continuous distribution function is sufficient to describe all the particles of some species s. This distribution function $f_s(\mathbf{x}, \mathbf{v}, t)$ describes how particles are distributed in both real space, and velocity space. The number of particles contained in a hyper-volume $d^3x d^3v$ located at $\mathbf{x}_0, \mathbf{v}_0$ are then described by $dN = f(\mathbf{x}_0, \mathbf{v}_0, t) d^3x d^3v$. We'd like to track the evolution of this distribution function. For a plasma with collisions the temporal evolution can be described by the Vlasov equation, which forms the fundamental basis of plasma physics. It takes on the following form,

$$\frac{\partial f_s}{\partial t} + \nabla \cdot (\mathbf{v} f_s) + \nabla_{\mathbf{v}} \cdot (\mathbf{a} f_s) = C_{ss'}. \tag{2.1}$$

Here:

$\mathbf{v}$ = a velocity vector in velocity space
$\mathbf{a}$ = an acceleration vector, the temporal derivative of $\mathbf{v}$
$\nabla_{\mathbf{v}}$ = Feynmann subscript notation for the gradient with respect to $\mathbf{v}$
$C_{ss'}$ = the collision operator, describing collisions between species s and s'

To make solving this equation more manageable, we prefer to track moments of the distribution function instead of the full function itself. We introduce the following averaging definition to abbreviate writing in taking these moments,

$$\begin{aligned} \langle \phi \rangle(\mathbf{x}, t) &= \frac{\int \phi f_s d^3v}{n_s}, \\ n_s(\mathbf{x}, t) &= \int f_s d^3v \end{aligned} \tag{2.2}$$

where the integral is taken over the entirety of velocity space. Furthermore,

ϕ = an arbitrary dyad
n_s = the number density.

We now multiply equation (2.1) by ϕ and average over velocity space. If one assumes that $\lim_{v\to\infty} \mathbf{a}\phi f_s = 0$, then the final expression can be simplified using integration by parts. This assumption should be checked for all cases, but as f_s usually scales as a Maxwellian (e^{-v^2}) the limit converges for any polynomial expression of ϕ. The equation reduces to

$$\frac{\partial n_s\langle\phi\rangle}{\partial t} + \nabla\cdot\langle n_s\phi\mathbf{v}\rangle - n_s\Big(\langle\frac{\partial\phi}{\partial t}\rangle + \langle\mathbf{v}\cdot\nabla\phi\rangle + \langle\mathbf{a}\cdot\nabla_{\mathbf{v}}\phi\rangle\Big) = n_s\Delta\phi. \tag{2.3}$$

Here, we define $n_s\Delta\phi$ to be the moment of the collision operator, i.e.

$$n_s\Delta\phi \equiv \int \phi C_{ss'} d^3v. \tag{2.4}$$

Using equation (2.3), one can quite readily derive important transport equations.

Density, momentum, and energy equations

To find the density equation, we set $\phi = 1$. This is equivalent to taking the zeroth moment of the distribution function with respect to velocity. This reduces equation (2.3) to

$$\frac{\partial n_s}{\partial t} + \nabla\cdot\langle n_s\mathbf{v}\rangle = n_s\Delta(1). \tag{2.5}$$

This is the mass continuity equation, with some source term determined by the collision operator (i.e. $n_s\Delta(1)$).

Using $\phi = m_s\mathbf{v}$ (with m_s being the particle mass) we retrieve the momentum equation,

$$\frac{\partial}{\partial t}(m_s n_s\langle\mathbf{v}\rangle) + \nabla\cdot(m_s n_s\langle\mathbf{v}\otimes\mathbf{v}\rangle) = n_s m_s\langle\mathbf{a}\rangle + n_s m_s\Delta\mathbf{v}. \tag{2.6}$$

Here, $\otimes$ denotes the dyadic product. Finally, we can retrieve the energy equation by setting $\phi = m_s v^2/2 = E_{T,s}$. This gives us

$$\frac{\partial n_s\langle E_{T,s}\rangle}{\partial t} + \nabla\cdot\langle n_s E_{T,s}\mathbf{v}\rangle = n_s m_s\langle\mathbf{a}\cdot\mathbf{v}\rangle + n_s\Delta E_{T,s}. \tag{2.7}$$

Equations (2.5), (2.6), and (2.7), are not in their canonical form yet. To write them in a more familiar form, we split up the velocity into a bulk flow and a deviation. Specifically, we set

$$\begin{aligned}\mathbf{v} &= \mathbf{u_s} + \mathbf{w},\\ \langle\mathbf{w}\rangle &= 0,\end{aligned} \tag{2.8}$$

where $\mathbf{u_s}$ is the plasma bulk flow and $\mathbf{w}$ is the deviation from the bulk flow. Furthermore, we introduce the convective derivative as

$$\Big(\frac{\mathrm{D}}{\mathrm{D}t}\Big)_s = \frac{\partial}{\partial t} + \mathbf{u_s}\cdot\nabla. \tag{2.9}$$

Using this convective derivative, the continuity, momentum, and energy equation can be respectively reduced to

$$\Big(\frac{\mathrm{D}n_s}{\mathrm{D}t}\Big)_s + n_s\nabla\cdot\mathbf{u_s} = n_s\Delta(1), \tag{2.10}$$

$$m_s n_s\Big(\frac{\mathrm{D}\mathbf{u_s}}{\mathrm{D}t}\Big)_s + \nabla\cdot\mathbf{P_s} + m_s n_s\mathbf{u_s}\Delta(1) = n_s m_s\langle\mathbf{a}\rangle + n_s m_s\Delta\mathbf{v}, \tag{2.11}$$

$$\begin{aligned} &n_s\Big(\frac{\mathrm{D}[m_s u_s^2/2 + 3T_s/2]}{\mathrm{D}t}\Big)_s + \nabla\cdot(\mathbf{P_s}\cdot\mathbf{u_s}) + \\ &\Big(\frac{1}{2}m_s u_s^2 + \frac{3}{2}T_s\Big)n_s\Delta(1) + \nabla\cdot\mathbf{q_s} = n_s m_s\langle\mathbf{a}\cdot\mathbf{u_s}\rangle + \frac{1}{2}n_s m_s\Delta v^2. \end{aligned} \tag{2.12}$$

Here,

$\mathbf{P_s} = m_s n_s\langle\mathbf{w}\otimes\mathbf{w}\rangle$, the pressure tensor
$\mathbf{q_s} = m_s n_s\langle w^2\mathbf{w}\rangle$, the heat flux
$T_s = m_s\langle w^2\rangle/3$, the thermal energy

These equations are still cumbersome, but they will simplify after we take a closer look at the collision terms.

Collisions

To make progress with simplifying the collision terms, we assume that the plasma consists of two fluids (hence it being called the two fluid model). This assumption can be broken if one accounts for impurities or neutrals in the plasma, but for simplicity's sake we will neglect these effects. One fluid will consist of electrons, and the other one of hydrogen ions, thus we will write down equations (2.10–2.12) for each of the species. Furthermore, we assume that only Lorentz forces are at play. Now our first assumption states that there is no source for electrons or ions. This would be broken if neutrals are taken into account, but we choose to neglect this effect. This means that the $\Delta(1)$ term will be zero. Secondly, since collision between like particles conserves momentum of given species, the only contribution to the $\Delta\mathbf{v}$ term will come from electron–ion collisions. Furthermore, the rate at which momentum is transferred from ions to electrons must be the same as the rate from electrons to ions. Quantatively,

$$\int(m_e\mathbf{v}C_{ei})d^3v = -\int(m_i\mathbf{v}C_{ie})d^3v = \mathbf{R}. \tag{2.13}$$

Here C_{ab} is the collision term describing how the distribution function of species a changes as it collides with species b. A similar argument holds for the collisions between species which transfer energy. Between like particles, no energy is transferred, while between unlike some energy is transferred. Since total energy is conserved, the rate at which energy is transferred from ions to electrons must equal the rate from electrons to ions. Thus,

$$\int (\frac{1}{2} m_e v^2 C_{ei}) d^3v = -\int (\frac{1}{2} m_i v^2 C_{ie}) d^3v = Q \tag{2.14}$$

We are now in a position to write out the full two-fluid equations.

Two-fluid equations

We now write out the continuity, momentum, and energy equations for a two component plasma. Furthermore, we use the fact that only the Lorentz force $\mathbf{F_L}$ is at play. We add in Maxwell's equations to find that the two-fluid equations reduce to

$$\begin{aligned}
\Big(\frac{\mathrm{D}n_i}{\mathrm{D}t}\Big)_i + n_i\nabla\cdot\mathbf{u_i} &= 0,\\
\Big(\frac{\mathrm{D}n_e}{\mathrm{D}t}\Big)_e + n_e\nabla\cdot\mathbf{u_e} &= 0,\\
m_i n_i\Big(\frac{\mathrm{D}\mathbf{u_i}}{\mathrm{D}t}\Big)_i + \nabla\cdot\mathbf{P_i} &= \mathbf{R} + n_i\mathbf{F_{L,i}},\\
m_e n_e\Big(\frac{\mathrm{D}\mathbf{u_e}}{\mathrm{D}t}\Big)_e + \nabla\cdot\mathbf{P_e} &= -\mathbf{R} + n_e\mathbf{F_{L,e}},\\
\frac{3}{2}n_i\Big(\frac{\mathrm{D}T_i}{\mathrm{D}t}\Big)_i + \mathbf{P_i}:\nabla\mathbf{u_i} + \nabla\cdot\mathbf{q_i} &= Q\\
\frac{3}{2}n_e\Big(\frac{\mathrm{D}T_e}{\mathrm{D}t}\Big)_e + \mathbf{P_e}:\nabla\mathbf{u_e} + \nabla\cdot\mathbf{q_e} &= -Q\\
\nabla\times\mathbf{E} &= -\frac{\partial\mathbf{B}}{\partial t}\\
\nabla\times\mathbf{B} &= \mu_0 e(n_i\mathbf{u_i} - n_e\mathbf{u_e}) + \frac{1}{c^2}\frac{\partial\mathbf{E}}{\partial t}\\
\nabla\cdot\mathbf{E} &= \frac{e}{\epsilon_0}(n_i - n_e)\\
\nabla\cdot\mathbf{B} &= 0
\end{aligned} \tag{2.15}$$

These equations form the basis of the two-fluid model, which are the equations employed by M3D-C1. We are now quite close to the form of the two-fluid equations that M3D-C1 uses, but we still require some additional caveats, for example a closure of the pressure tensor. Firstly, the plasma is assumed to be quasi-neutral implying that $n_i = n_e$. The pressure tensor is split up into an anisotropic and isotropic part:

$$\mathbf{P_s} = p_s\mathbf{I} + \mathbf{\Pi}_s. \tag{2.16}$$

It is easy to show that $p_s = n_s T_s$. Furthermore, we use the fact that $m_e \ll m_i$. In turn we prefer to solve not for the electron velocity, but for the current and ion velocity. This is preferable, as current is more easily measured. These are defined by

$$\begin{aligned}
\mathbf{u_i} &= \mathbf{u}\\
\mathbf{J} &= en(\mathbf{u} - \mathbf{u_e}).
\end{aligned} \tag{2.17}$$

Additionally we assume that all timescales are large enough that we can neglect the displacement current in Maxwell's equations. Finally, the closures for $\mathbf{R}$, $\mathbf{\Pi}$, $\mathbf{q}$, and Q need to be chosen as well. These take the form as can be seen in equations 2.19. These closures are elaborated in N. Ferraro's 2009 paper [22], but most of them derive from Braginskii's 1965 paper [20]. Using all these closures, the final form of

the two-fluid equations are found to be

$$\begin{aligned}
\Big(\frac{\mathrm{D}n_i}{\mathrm{D}t}\Big) + n_i\nabla\mathbf{u} = & \quad 0, \\
m_i n_i\Big(\frac{\mathrm{D}\mathbf{u}}{\mathrm{D}t}\Big) = & \quad \mathbf{J}\times\mathbf{B} - \nabla(p_i+p_e) - \nabla\cdot\mathbf{\Pi}_i, \\
\Big(\frac{\mathrm{D}(p_i+p_e)}{\mathrm{D}t}\Big) + \Gamma(p_i+p_e)\nabla\cdot\mathbf{u} = & \quad (\Gamma-1)(\eta J^2 - \nabla\cdot\mathbf{q} - \mathbf{\Pi}_i:\mathbf{u}) + \\
& \quad \frac{1}{n_i e}\mathbf{J}\cdot\Big(\nabla p_e - \Gamma\frac{\nabla n_i}{n_i}p_e\Big), \\
\Big(\frac{\mathrm{D}p_e}{\mathrm{D}t}\Big) + \Gamma p_e\nabla\cdot\mathbf{u} = & \quad (\Gamma-1)(\eta J^2 - \nabla\cdot\mathbf{q_e}) + \\
& \quad \frac{1}{n_i e}\mathbf{J}\cdot\Big(\nabla p_e - \Gamma\frac{\nabla n_i}{n_i}p_e\Big), \\
\frac{\partial\mathbf{B}}{\partial t} = & \quad -\nabla\times\mathbf{E}, \\
\mathbf{E}+\mathbf{u}\times\mathbf{B} = & \quad \eta\mathbf{J} + \frac{1}{n_i e}(\mathbf{J}\times\mathbf{B} - \nabla p_e)
\end{aligned} \tag{2.18}$$

with

$$\begin{aligned}
\mathbf{\Pi}_i = & \quad -\mu(\nabla\mathbf{v} + [\nabla\mathbf{v}^T]), \\
\mathbf{q} = & \quad -\kappa\nabla(T_e+T_i) \\
\mathbf{q_e} = & \quad -\kappa\nabla T_e - \kappa_\parallel\frac{\mathbf{B}\otimes\mathbf{B}}{B^2}\cdot\nabla T_e, \\
\Gamma = & \quad \frac{5}{3}
\end{aligned} \tag{2.19}$$

A straightforward derivation of the ion anisotropic tensor closure can also be found in Batchelor [23]. These closures can also be interpreted as diffusion equations, where μ is a factor dictating the momentum diffusivity, κ is a factor dictating the heat diffusivity perpendicular to field lines, and $\kappa_\parallel$ is a factor dictating heat diffusivity parallel to the field lines. It is important to note that κ and μ can be arbitrary functions of the location. The specific form of these functions is left as a choice (one could for example use a constant factor κ). The set of equations (2.18) are the equations M3D-C1 evolves.

2.2 Mode penetration

We now take a section to describe the analytical theory behind mode-penetration, as derived by Fitzpatrick in 1993 [15]. As the phenomenon is inherently non-linear, it requires quite a bit a algebra and footwork. To facilitate the interpretation of this calculation, we first present a novel heuristic model. This model is meant to exemplify the essentials of mode-penetration, with a strong focus on the physics. After this, a formal derivation of the mode-penetration phenomenon is given.

2.2.1 Heuristic model

We shall understand this heuristic model by breaking it up into three parts: a sketch of the set-up, an introduction of the forces acting on the plasma, and finally the derivation of mode-penetration itself.

The set-up

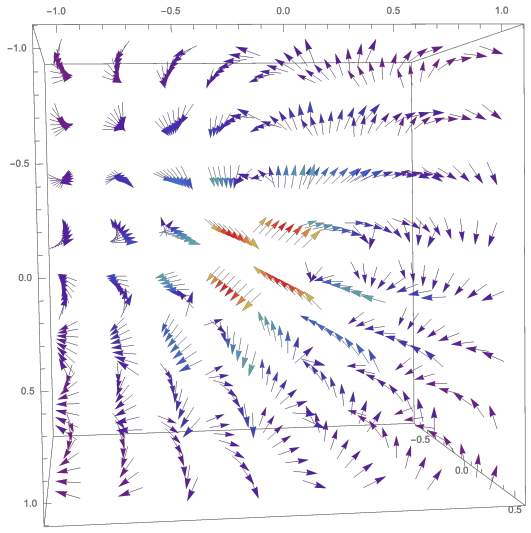

Figure 2.1: Example of a perturbing vector field, with mode number $(m = 2, n = 1)$, in a straight cylinder tokamak with major radius $R_0 = 4$. In straight cylinder geometry the major radius encapsulates the length over which the cylinder is periodic. Thus after traversing 4 meters across the axial (or toroidal) extent of the circle, the cylinder is the same. The toroidal direction is the one going into the page. The mode number can be deduced by observing that the vectors are symmetric under half of a full poloidal rotation in a poloidal cross-section. The toroidal mode number (n) can be deduced by observing that after traversing a quarter of the total toroidal distance (which is the toroidal extent plotted here), vectors have rotated a quarter of a full circle. This implies that after traversing the entire toroidal axis, vectors will have rotated once meaning that $n = 1$. This plot was generated by using the function $\mathbf{B} = \mathrm{Re}\left[\nabla \times (e^{-r^2} \cdot e^{i\cdot(m\theta - 2\pi n z/R_0)}\hat{z})\right]$, which is divergence free.

The scenario we will be focusing on is the following. Suppose we have a cylindrically symmetric plasma, with a purely axial (or "toroidal", in a straight tokamak sense) flow profile present. We now perturb the plasma with some (m, n) perturbation. This perturbation can best be thought of as adding some small Fourier components

in the poloidal and toroidal direction. The periodicity of this Fourier component is characterized by the symmetry in both the poloidal and toroidal direction. If the perturbing vector field is invariant under $2\pi/n$ of a poloidal rotation, the poloidal mode number is n. If the perturbing vector field is invariant under an axial translation of R_0/m, the toroidal (or axial) mode number is m. This is exactly what (m, n) characterizes: m is the translation symmetry in the axial direction, whereas n is rotational symmetry in the poloidal direction. An exemplary perturbing vector field is given in figure 2.1.

The presence of this perturbation will in turn give rise to an (m, n) magnetic island chain forming on the resonant surface (the resonant surface is the locations where the safety factor q is equal to m/n). Magnetic islands are regions of the magnetic field that are distinct from the rest of the plasma: a magnetic field line within a magnetic island will always stay within it, and is bounded by the separatrix. As mentioned in the introduction, outside the magnetic island field lines form nested surfaces around the magnetic axis. Within the island, the magnetic field lines form nested surfaces around a single magnetic field line which also resides in the island. The separatrix defines the boundary between these two differing behaviours. A sketch of a magnetic island chain is given in figure 2.2.

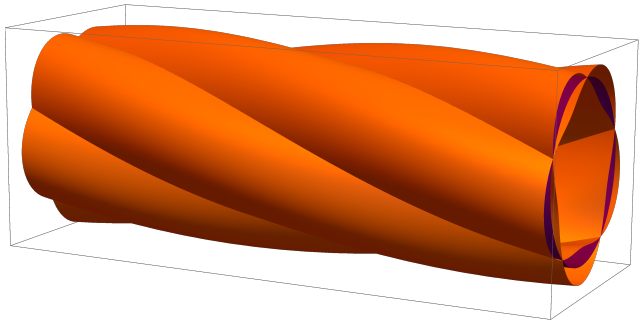

Figure 2.2: A $(5, 1)$ magnetic island chain. The island separatrix is shown in orange, and the resonant surface in purple. It can be seen that the surface is periodic in the toroidal direction.

Now an interesting peculiarity of the island separatrix, is that there is no flow of plasma across it, a results found in 1991 by Fitzpatrick [24]. This has the consequence that our magnetic island chain can effectively be treated as a solid body entrenched in a fluid. The plasma has a velocity relative to the island, meaning that the island chain experiences a net viscous force pulling on it. This force will pull the island out of the position where it originally formed.

However the (m, n) perturbation which gave rise to the island stays in its original position. Normally the perturbation and the magnetic island align perfectly, but because of the viscous force pulling on the island they now have a certain phase difference. This is exemplified in figure 2.3. The phase difference means that flux surfaces no longer align with the perturbations. Switching to a reference frame that is co-moving with the plasma velocity, this is equivalent to a conductor which is placed in a varying magnetic field. From Faraday's law of induction we know that a changing magnetic field must give rise to electric fields. These electric fields in turn give rise to so-called eddy currents in the plasma, simply through Ohm's law $\mathbf{E} = \eta \mathbf{J}$.

These eddy currents in turn interact with the magnetic field, giving rise to $\mathbf{J} \times \mathbf{B}$ forces which tend to push the magnetic island back to its equilibrium position. This is where the non-linearity comes into play - perturbed fields give rise to perturbed currents, which in turn interact with the perturbed field again.

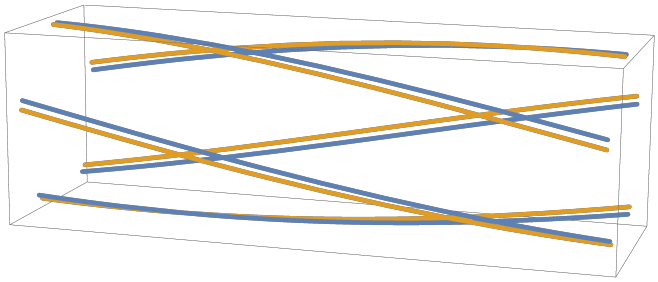

Figure 2.3: A phase difference between the magnetic islands and the perturbation which gave rise to it. The lines in this plot represent the centre of the magnetic island after the phase shift (orange), and the places where the perturbation is the strongest on the resonant surface (blue). It can be seen that the blue lines are lagging slightly behind the orange ones. The size of this gap is related to the phase shift.

The forces

We are interested in the equilibrium of this force balance. What is the final outcome of this battle between electro-magnetic and viscous forces? To make progress it is important to realize that both the viscous force and the electromagnetic forces are functions of plasma velocity. There are certain caveats to both forces, and we shall investigate the viscous force first.

The first important fact of the viscous force that is readily obtained is the fact that it scales linearly with the plasma velocity. However, there is still an important degree of freedom left in the system. The plasma within the magnetic island chain can have some non-zero velocity. This affects the total viscous force, as it is the difference in velocity that matters for the viscous force. We fix this island velocity to some non-zero value [25], meaning that at zero plasma velocity, there is a non-zero viscous force present. This means that the viscous force as a function of the plasma velocity is a translated straight line.

Next we shift our attention to the electromagnetic force. This force is dictated by three different parameters,

$$|\mathbf{J} \times \mathbf{B}| = |\mathbf{J}||\mathbf{B}| \sin(\Delta\phi). \tag{2.20}$$

Here $\mathbf{B}$ is the full magnetic field (including the perturbation). We start by investigating the $|\mathbf{J}||\mathbf{B}|$ quantity, excluding the $\sin(\Delta\phi)$ term. To be clear, $\Delta\phi$ is the phase shift and not the previously mentioned moment of the collision operator. When there is no plasma velocity, the external perturbation will give rise to an response field in the plasma (magnetic islands and such). This response field will ensure that $\mathbf{J} \times \mathbf{B}$ is in force balance within the plasma, but the the $|\mathbf{J}||\mathbf{B}|$ component itself need not be zero. Small modulations of plasma velocity only barely effect the magnitude of $|\mathbf{J}||\mathbf{B}|$, and the field stays constant. In the fast flowing regime however (so fast plasma flows), eddy currents (currents which arise due to the fluctuating magnetic fields) will be the dominant response to the external perturbation. To see how the

force magnitude scales with plasma velocity, we make use of a simple toy-model. This model is not meant to perfectly represent our system, but it exemplifies the screening-out effect from eddy currents.

Adopting a frame of reference that is co-moving with the plasma bulk flow, the external perturbation becomes a temporally modulated magnetic field with a frequency proportional to the plasma velocity which we shall call ω. We model the plasma as an infinite conducting slab. We would like to find the response field to this modulating external field. To do so, we make use of Maxwell's equations, in combination with Ohm's law:

$$\begin{aligned} \frac{\partial(\mathbf{B_{ext}} + \mathbf{B_{res}})}{\partial t} &= -\nabla \times \mathbf{E}, \\ \mathbf{E} &= \eta \mathbf{J_{res}}, \\ \nabla \times \mathbf{B_{res}} &= \mu_0 \mathbf{J_{res}}. \end{aligned} \tag{2.21}$$

Here $\mathbf{B_{ext}}$ is the external perturbation and $\mathbf{B_{res}}$ is the response field. Imposing that $\mathbf{B_{ext}} = B_0 e^{i(kx-\omega t)}\hat{z}$, one can readily show that

$$\begin{aligned} \mathbf{B_{res}} &= -\frac{B_0}{1 + i\eta k^2/\mu_0\omega} e^{i(kx-\omega t)}\hat{z}, \\ |\mathbf{J_{res}}||\mathbf{B_{ext}} + \mathbf{B_{res}}| &= \frac{kB_0^2}{\mu_0} \frac{\eta k^2/\mu_0\omega}{1 + (\eta k^2/\mu_0\omega)^2}. \end{aligned} \tag{2.22}$$

Here, k is a typical inverse lengthscale. In the fast frequency limit (so a fast flowing plasma) the $|\mathbf{J}||\mathbf{B}|$ quantity scales as $1/\omega$.

We now investigate the steady state behaviour of $\sin(\Delta\phi)$. The angle $\Delta\phi$ is directly related to the angle between the magnetic islands and the perturbation giving rise to it. When there is no velocity present this angle is zero. For low velocities, the angle scales linearly with plasma velocity. This cannot continue indefinitely, because if the angle *would* keep growing unbounded with plasma velocity the island phase would loop back on itself at some point. This would mean that the island could go on to repeat this behaviour indefinitely never converging to an equilibrium. Thus it must grow to some value asymptotically with ever increasing plasma velocity. Combining these two behaviours, we find that the electromagnetic force scales linearly with plasma velocity in the low-velocity regime, and decreases towards zero in the high velocity regime.

The last caveat to the forces is understanding how it scales with the perturbation strength. Equation (2.22) indicates a squared scaling with the perturbation strength for the electromagnetic force, and this does indeed hold in all regimes. This is because the induced currents in both the low velocity and high velocity regime scale with the perturbation strength, meaning that the total force also goes with the square of the perturbation. The viscous force however is independent of the perturbation strength.

Mode-penetration

We now combine all these different scaling laws to understand the equilibrium behaviour of the plasma. A plot of the electromagnetic and viscous force as a function of perturbation strength and plasma velocity is given in figure 2.4. Fixing the

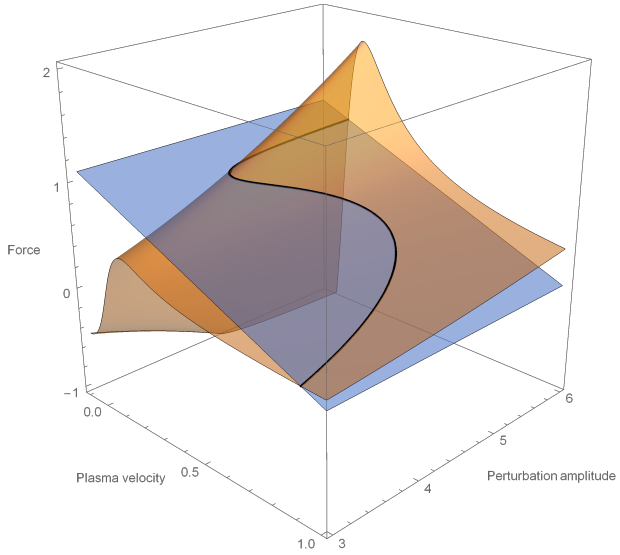

Figure 2.4: The surfaces describing the electromagnetic force (orange) and the viscous force (blue). The plasma is in equilibrium if these two forces are equal, and this equilibrium solution is highlighted in black.

perturbation strength, we see that there are three distinct behaviours for plasma equilibria.

For low perturbation strengths a single solution exists where both forces are equal. This solution has a fast plasma velocity. This solution will be coined the “fast” solution branch. For high perturbation strengths, there is again a single solution. This solution has a very low plasma velocity compared to the fast solution. It will thus be coined the “slow” solution branch. For intermediate perturbation strengths, a third solution comes into play. This new solution is inaccessible because it is unstable. This can best be understood by taking some point on this intermediate solution and slightly perturbing the plasma velocity. A slight increase of plasma velocity means that the viscous force wins (so it is stronger than the electro-magnetic force), pulling the islands even further from equilibrium. A slight decrease in plasma velocity means that the electromagnetic force wins, further pulling the island inward. Similar argumentation can be used to show that the fast and slow solutions are stable.

This instability means that there is no way to go from the slow solution branch to the fast one in a continuous, reversible manner. They can only be accessed dynamically. It is the sudden jump from a high plasma velocity to a low one that is coined the mode-penetration. This bifurcation happens at some critical value of the perturbation strength, B_{crit}.

To account for external forces (supplied by NBIs or other means) near the magnetic island, we additionally introduce an extra force into this force balance. Assuming this force is only weakly dependent on plasma velocity and perturbation strength, this new force can be interpreted as an offset to the viscous force (i.e. a translation in the Force direction in figure 2.4 of the blue surface). This offset can be

used to control the threshold perturbation amplitude at which mode-penetration occurs.

After this investigation into the heuristic model, we will look into the actual theory behind mode-penetration. We will start by deriving the central equation which contains the information on how plasma interacts with external responses, modelled as perturbations - the tearing mode equation

2.2.2 Tearing mode theory

To derive the tearing mode equation we start with the central equation for plasma equilibria, which follows from (2.18). We assume an ideal-MHD equilibrium, meaning that

$$\mathbf{J} \times \mathbf{B} = \nabla p \Rightarrow \nabla \times (\mathbf{J} \times \mathbf{B}) = 0. \tag{2.23}$$

Making use of vector calculus identities, and the incompressibility of magnetic and current fields, one can expand the identity into an easier form. It reduces to

$$(\mathbf{B} \cdot \nabla)\mathbf{J} - (\mathbf{J} \cdot \nabla)\mathbf{B} = 0. \tag{2.24}$$

We linearize the equations by introducing equilibrium and perturbed quantities. We substitute the magnetic and current fields as

$$\begin{aligned} \mathbf{B} \rightarrow &\quad \mathbf{B_0} + \delta\mathbf{B}, \\ \mathbf{J} \rightarrow &\quad \mathbf{J_0} + \delta\mathbf{J}. \end{aligned} \tag{2.25}$$

Neglecting the second order quantities, and excluding equilibrium quantities (because they already solve equation (2.23)) one finds

$$(\delta\mathbf{B} \cdot \nabla)\mathbf{J}_0 + (\mathbf{B}_0 \cdot \nabla)\delta\mathbf{J} - \big[(\delta\mathbf{J} \cdot \nabla)\mathbf{B}_0 + (\mathbf{J}_0 \cdot \nabla)\delta\mathbf{B}\big] = 0. \tag{2.26}$$

We take the equilibrium magnetic field to be of the following form

$$\mathbf{B_0} = B_\theta(r)\hat{\theta} + B_z\hat{z} \Rightarrow \mathbf{J}_0 = \frac{1}{\mu_0 r}\frac{\partial(rB_\theta)}{\partial r}\hat{z}. \tag{2.27}$$

Here, r is the distance from the magnetic axis, θ is the poloidal angle, and z is axial or toroidal direction. Furthermore, the perturbations are assumed to be of the following form

$$\delta\mathbf{B}(r, \theta, z) = \delta\mathbf{B}(r)e^{i\xi} \tag{2.28}$$

Here $\xi = m\theta - nz/R_0$. This form is chosen because it is a single mode of a Fourier decomposition of an arbitrary perturbation, so we can respresent any perturbation as a sum of arbitrary modes. We also take that the axial component (the $\hat{z}$ component) of $\delta\mathbf{B}$ is negligible compared to the other components. This arises due to the fact that the field arising from the coils is usually dominant, but the assumption does not hold in general. This allows us to write $\delta\mathbf{B}$ in terms of a flux-function ψ. This is due to the incompressibility of the magnetic field, analogous to how one defines a flow potential in incompressible flows. We rewrite the perturbed field as

$$\delta\mathbf{B} = \nabla \times (\psi\hat{z}), \tag{2.29}$$

where $\psi = \psi(r)e^{i\xi}$. Using the fact that $\nabla \times \mathbf{B} = \mu_0\mathbf{J}$, equation (2.26) can be written in terms of the flux function. We introduce the shorthand

$$\nabla^2_{r,\theta}\psi \equiv \frac{1}{r}\frac{\partial}{\partial r}\Big(r\frac{\partial\psi}{\partial r}\Big) - \frac{m^2}{r^2}\psi. \tag{2.30}$$

This allows us to write out the equations from (2.26) as:

$$\begin{aligned} \mu_0 \delta \mathbf{J} = &\quad -i\frac{n}{R_0}\frac{\partial \psi}{\partial r}\hat{r} + \frac{nm}{rR_0}\psi\hat{\theta} - \nabla^2_{r,\theta}\psi\hat{z}m \\ \nabla^2_{r,\theta}\psi = &\quad -\frac{\frac{m}{n}\mu_0 J'_z(r)}{B_\theta\left[\frac{B_z r}{B_\theta R_0} - \frac{m}{n}\right]}. \end{aligned} \tag{2.31}$$

Here $j_z = \mathbf{J_0} \cdot \hat{z}$. The last equation of (2.31) is the well-known tearing mode equation. We simplify it by introducing the safety factor, and the resonant surface safety factor. We find

$$\nabla^2_{r,\theta}\psi(r) + \frac{\mu_0 J'_z}{B_\theta}\frac{q_s}{q - q_s}\psi(r) = 0 \tag{2.32}$$

where:

$$\begin{aligned} q &= B_z r / B_\theta R_0, \\ q_s &= m/n. \end{aligned}$$

This equation describes how the perturbed magnetic field depends on equilibrium quantities like the rotational transform, and the axial current. We see that this tearing mode equation has a singular point at $q = q_s$. To interpret what this means, we investigate the behaviour of the current near this singular point. From (2.31) we see that the current also diverges near this singular point. This indicates that ideal MHD is no longer a valid approximation, as resistive effects will become important. We assume that ideal MHD holds for the region where $r \notin [r_{s-}, r_{s+}]$. The regions are stitched together using the constant-ψ approximation, which assumes that $\psi(r_{s-}) = \psi(r_{s+}) = \psi_s$. Finally, we require two boundary conditions to fully solve the tearing mode equation. We assume that the flux function is well behaved near the magnetic axis and vanishes at infinity. Thus,

$$\psi(0) = 0, \qquad \psi(\infty) = 0. \tag{2.33}$$

We now inspect some essential features of the tearing mode equation.

Vacuum solutions

We inspect the vacuum solutions of the tearing mode equation, (2.32). These can be obtained by setting $J'_z(r) = 0$. The equation reduces to

$$\frac{1}{r}\frac{\partial}{\partial r}\left(r\frac{\partial \psi}{\partial r}\right) = \frac{m^2}{r^2}\psi. \tag{2.34}$$

Using the substitution $\psi(\ln r)$, the equation takes the simple form

$$\psi(r) = ar^{-m} + br^m, \tag{2.35}$$

where a and b are constants set by boundary conditions. These vacuum solutions are much easier to work with than the full tearing mode equation, and are a valid approximation in systems where current is very peaked. If one is outside this peaked current region, the vacuum solutions are close to the true solutions to the tearing mode equation.

Rutherford stability parameter

We dedicate a short section to stability of a perturbation, as this will be relevant for the result. An important parameter arising from the tearing mode equation, is the so-called Rutherford stability parameter. In Rutherford's 1973 paper he showed that the jump in derivatives near the singular surface determines the stability of the mode [26]. The typical definition for this parameter is

$$\Delta' = \frac{1}{\psi_s}\left[\frac{\partial\psi(r)}{\partial r}\right]_{r_{s-}}^{r_{s+}}. \tag{2.36}$$

Rutherford found that for $\Delta' > 0$ the mode is unstable, whereas for $\Delta' < 0$ the mode is stable. The stability means that ψ stays bounded for stable modes, whereas is grows for unstable modes. This in turn means that the island width, which is goes as $\sqrt{\psi}$, grows for $\Delta' > 0$, whereas it stays bounded for $\Delta' < 0$. We will now derive this dependence on ψ for the island size.

Magnetic islands and island width

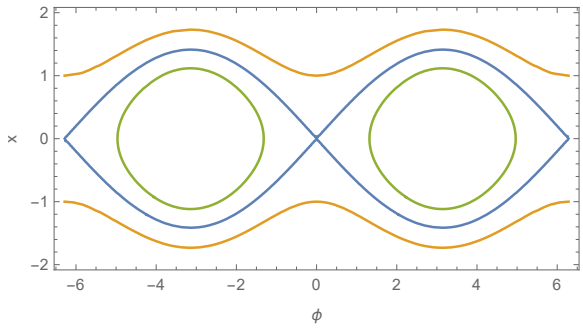

Figure 2.5: A plot showing different solutions to equation (2.40). The island separatrix can be seen in blue. The orange solution is outside the magnetic island, whereas the green one is within it. These regions are distinct.

To relate the flux function to magnetic islands, we use the fact that the helical flux is a conserved quantity [27]. The helical flux is defined by the following differential equation,

$$\frac{\partial \psi_*}{\partial r} = B_* \equiv B_\theta (1 - \frac{q}{q_s}). \tag{2.37}$$

In this section, B_θ entails the perturbation as well. We Taylor expand this expression to first order around the resonant surface, r_s. Introducing the shear as $s = (r/q)\partial q/\partial r$ the helical magnetic field reduces to

$$\frac{\partial \psi_*}{\partial r} = -\frac{B_z s_s}{R_0 q_s}(r - r_s) + \frac{\partial \psi}{\partial r}. \tag{2.38}$$

The ψ component refers to the perturbed part, as defined in equation (2.29). Substituting in $x = r - r_s$, we find

$$\psi_* = -\frac{1}{2}\frac{B_z s_s}{R_0 q_s} x^2 + \psi \Rightarrow x^2 = -\frac{2R_0 q_s}{B_z s_s}\Big[\psi_* - \psi\Big]. \tag{2.39}$$

If we choose the same helical mode number as the perturbation, ψ reduces to some function $\psi(r)$ multiplied by some phase factor $e^{i\varphi}$. This phase factor depends on which helical surface we choose. Substituting in this result returns,

$$x^2 = \frac{2R_0 q_s |\psi|}{B_z s_s}\Big[\frac{\psi_*}{\psi_1} - \cos(\varphi)\Big]. \tag{2.40}$$

Taking ψ to be roughly constant within the magnetic island (which is the constant-ψ approximation), there is a family of solutions, for different values of ψ_*. A plot showing some solutions can be seen in figure 2.5. On the separatrix $\psi = \psi_*$, and the island width is easily calculated to be

$$W = 4\sqrt{\frac{R_0 q_s |\psi|}{B_z s_s}}. \tag{2.41}$$

Here we see the relation between the magnetic flux function and the island width. Thus, if the flux function grows over time, so does the magnetic island.

2.2.3 The electromagnetic force

Here, we calculate a general expression for the electromagnetic force. This will be useful, as in the force balance this electromagnetic force has to be balanced against the viscous force. It turns out that torque is a slightly more natural quantity to look at instead of force, due to $1/r$ terms appearing in forces. The first important realisation is that in ideal MHD equilibrium all torque comes from jumps in derivatives. This can be seen by investigating the ideal MHD equilibrium equation $\mathbf{J} \times \mathbf{B} = \nabla p$. We rewrite it to,

$$\begin{aligned} T_{\theta,EM} &= \int r(\mathbf{J} \times \mathbf{B}) \cdot \hat{\theta} dV = \int \frac{\partial p}{\partial \theta} dV, \\ T_{z,EM} &= R_0 \int (\mathbf{J} \times \mathbf{B}) \cdot \hat{z} dV = R_0 \int \frac{\partial p}{\partial z} dV. \end{aligned} \tag{2.42}$$

Here the T quantities denote torque. Because of the periodicity of p (pressure) in z and θ, this can only be non-zero if there are jumps in derivatives. We fill in the perturbed quantities, and realise that all first order terms contain a $e^{i\xi}$ term. The first order terms will average to zero in the integration, so only the second order terms will survive. We keep in mind that we always take the real part of these complex quantities. Writing out the product of the real parts (instead of the real part of the product), the surviving terms are

$$\begin{aligned} T_{\theta,EM} = &\quad \frac{1}{4}\int r(\delta\mathbf{J}^* \times \delta\mathbf{B} + \delta\mathbf{J} \times \delta\mathbf{B}^*) \cdot \hat{\theta} dV, \\ T_{z,EM} = &\quad \frac{R_0}{4}\int (\delta\mathbf{J}^* \times \delta\mathbf{B} + \delta\mathbf{J} \times \delta\mathbf{B}^*) \cdot \hat{z} dV. \end{aligned} \tag{2.43}$$

Here * denotes complex conjugation. Carrying out the cross products, and remembering that $\delta\mathbf{B}$ has no $\hat{z}$ component, the cross products become

$$\begin{aligned} T_{\theta,EM} &= \frac{1}{4}\int r(\delta j_z^* \delta B_r + \delta j_z \delta B_r^*) dV, \\ T_{z,EM} &= \frac{R_0}{4}\int (\delta j_r^* \delta B_\theta + \delta j_r \delta B_\theta^* - \delta j_\theta^* \delta B_r - \delta j_\theta \delta B_r^*) dV. \end{aligned} \tag{2.44}$$

Using equation (2.29) and integrating by parts, the two components become,

$$\begin{aligned} T_{\theta,EM} &= 4\pi^2 R_0 \frac{m}{\mu_0}\frac{i}{4}\left(\Big[r\frac{\partial\psi}{\partial r}\Big]_{r_{k-}}^{r_{k+}} \psi_k^* - \Big[r\frac{\partial\psi^*}{\partial r}\Big]_{r_{k-}}^{r_{k+}} \psi_k \right), \\ T_{z,EM} &= -\frac{1}{q_s} T_{\theta,EM} + \int R_0 \Big(r\delta j_r'^* B_r + r\delta j_r' B_r^* \Big) dV. \end{aligned} \tag{2.45}$$

Here the last integral term is simplified using current conservation. Now, we impose the constant-ψ approximation to neglect the integral term in equation (2.45).

Interaction of the force with the island

To calculate the interaction of an external mode with the magnetic island, we will split up the magnetic flux function (the flux function that solves $\delta\mathbf{B} = \nabla \times (\psi\hat{z})$) into two parts. One part, ψ_{mode}, represents purely the tearing mode, without any effect of the external coil. The second part, ψ_{coil}, represents the ideal MHD response to the external perturbation caused by the coil. To make progress in solving this complex equation, we assume that most current is located at small radii $r < r_{k+}$, so that we can use the vacuum solutions from equation (2.35) in this region.

Firstly, we try to find an expression for ψ_{mode}. At $r = r_{k+}$ we make use of the constant-ψ approximation to set the boundary condition $\psi(r_{k+}) = \psi_k$. Since it is unaffected by the external structure, the second boundary condition is simply $\psi(\infty) = 0$. Using the vacuum equation we find the solution

$$\psi_{mode}(r) = \psi_k \Big(\frac{r_{k+}}{r} \Big)^m. \tag{2.46}$$

Now the second equation describing ψ_{coil} is a bit more complicated. The first boundary condition is set by realizing that in ideal MHD, the resonant surface will try to screen out the external perturbation by screening currents. This means that $\psi_{coil}(r = r_{k+}) = 0$. The second boundary condition is simply that $\psi(\infty) = 0$. But, since there is current flowing at the coil location, there is a jump in the magnetic flux function at this coil location r_c. To calculate this jump we will look at another magnetic flux function first, namely that of the coil without a plasma present. This function ψ_{vac} upholds three boundary conditions, namely

$$\psi_{vac}(r = 0) = 0, \qquad \psi_{vac}(r = r_c) = \psi_c, \qquad \psi_{vac}(r = \infty) = 0. \tag{2.47}$$

Here ψ_c is related to the amount of current flowing in the coil. Using the vacuum solutions we find

$$\begin{cases} \psi_{vac} = \psi_c \left(\frac{r}{r_c}\right)^m & r \in [0, r_c), \\ \\ \psi_{vac} = \psi_c \left(\frac{r_c}{r}\right)^m & r \in [r_c, \infty). \end{cases} \tag{2.48}$$

The jump across the coil surface is easily calculated to be

$$\left[\frac{\partial \psi_{vac}}{\partial r}\right]_{r_{c-}}^{r_{c+}} = 2m\frac{\psi_c}{r_c} \tag{2.49}$$

Since there is no plasma flowing at the coil location, the jump in derivatives has to be the same. Using this as a matching condition we find

$$\begin{cases} \psi_{coil} = 0, & r \in [0, r_{k+}) \\ \\ \psi_{coil} = \psi_{vac}(r_{k+})\left(\frac{r^m}{r_{k+}^m} - \frac{r_{k+}^m}{r^m}\right), & r \in [r_{k+}, r_c) \\ \\ \psi_{coil} = \psi_{vac}(r_{k+})\left(\frac{r_c^m}{r_{k+}^m} - \frac{r_{k+}^m}{r_c^m}\right)\frac{r_c^m}{r^m}, & r \in [r_c, \infty). \end{cases} \tag{2.50}$$

Now that we have finally acquired the two flux functions we combine them simply by adding them with some phase difference,

$$\psi = \psi_{mode} e^{i\xi + i\Delta\varphi} + \psi_{coil} e^{i\xi}. \tag{2.51}$$

Using this, we can calculate the Rutherford stability parameter to be

$$\begin{aligned} \Delta' &= \Delta'_{mode} + \Delta'_{coil} \\ \Delta'_{coil} &= 2m\frac{\psi_{vac}(r_{k+})}{\psi_k}\frac{1}{r_{k+}}e^{-i\Delta\varphi}. \end{aligned} \tag{2.52}$$

Using these flux functions, the electromagnetic force can be found to be

$$T_{\theta,EM} = -4\pi^2 R_0 \frac{m^2}{\mu_0}\psi_k \psi_{vac}(r_{k+}) \sin\Delta\varphi. \tag{2.53}$$

2.2.4 Viscous forces

We now dedicate a section to the calculation of the viscous forces, which will compete with the electromagnetic forces. The viscous forces will be modelled by making use of the closure explained by Batchelor [23]. Here, the viscous force densities $\mathbf{f_v}$ are shown to be

$$\mathbf{f_v} = \nabla \cdot \left\{ \mu \Big[\nabla \mathbf{u} + (\nabla \mathbf{u})^T \Big] \right\}. \tag{2.54}$$

This is equation is essentially telling us that gradients in the velocity field will give rise to forces, and the strength of this force is proportional to the viscosity. We will slightly adjust the equations by rewriting them in terms of fluid frequency instead of velocity, as this will simplify these equations a great deal. These frequencies are defined by

$$u_\theta = r\Omega_\theta, \qquad u_z = R_0 \Omega_z. \tag{2.55}$$

Using this, the poloidal and axial components of this force can be found to be

$$\begin{aligned} \mathbf{f_v} \cdot \hat{\theta} &= \frac{1}{r^2} \frac{\partial}{\partial r} \Big(\mu r^3 \frac{\partial \Omega_\theta}{\partial r} \Big), \\ \mathbf{f_v} \cdot \hat{z} &= \frac{R_0}{r} \frac{\partial}{\partial r} \Big(\mu r \frac{\partial \Omega_z}{\partial r} \Big). \end{aligned} \tag{2.56}$$

From here, we integrate over across the region containing the magnetic island to find the torque. This is then evaluated to be

$$\begin{aligned} T_{\theta,VS} &= 4\pi^2 R_0 \Big[\mu r^3 \frac{\partial \Omega_\theta}{\partial r} \Big]_{r_{s-}}^{r_{s+}}, \\ T_{z,VS} &= 4\pi^2 R_0^3 \Big[\mu r \frac{\partial \Omega_z}{\partial r} \Big]_{r_{s-}}^{r_{s+}}, \end{aligned} \tag{2.57}$$

Here r_s stands for the radial value of the separatrix. The viscous forces are thus related to the jumps in the profiles across the magnetic island. We fix the rotation speed of the magnetic island to

$$\begin{aligned} \Omega_\theta(r_s) &= \Omega_{\theta,0}, \\ \Omega_z(r_s) &= \Omega_{z,0}. \end{aligned} \tag{2.58}$$

This allows us to solve the equation, subject to three conditions. We impose that the profiles are well-behaved on-axis, meaning that $\Omega'_\theta(0) = \Omega'_z(0) = 0$. Finally, we fix the edge value to uphold a no-slip condition, meaning that $\Omega_\theta(a) = \Omega_z(a) = 0$. For the driving term of the differential equation (so the term which will drive fluid velocities), we take a novel approach. The poloidal part will have no driving term, but the toroidal (or axial) part will contain a driving term (e.g. neutral beam injection). The driving term will be written as being proportional to some arbitrary function $f(r)$. This will slightly modify the equation. We solve the equations given in (2.56) to find

$$\begin{cases} \Omega_\theta(r) = \Omega_{\theta,0} & r \in [0, r_{s-}), \\ \Omega_\theta(r) = \Omega_{\theta,0} \frac{\int_r^a (\mu r'^3)^{-1} dr'}{\int_{r_{s+}}^a (\mu r'^3)^{-1} dr'} & r \in [r_{s+}, a). \end{cases} \tag{2.59}$$

$$\begin{cases} \Omega_z(r) = \Omega_{z,0}(1 + \kappa_F \int_r^{r_{s-}} \frac{g_0(r')}{\mu r'} dr') & r \in [0, r_{s-}), \\ \Omega_z(r) = \Omega_{z,0}\Big(\frac{\int_r^a (\mu r')^{-1} dr'}{\int_{r_{s+}}^a (\mu r')^{-1} dr'} - \kappa_F \int_r^a \frac{g(r')}{\mu r'} dr' + \kappa_F \frac{\int_{r_{s+}}^a g(r') dr'/\mu r'}{\int_{r_{s+}}^a dr'/\mu r'} \int_r^a \frac{dr'}{\mu r'} \Big) & r \in [r_{s+}, a). \end{cases} \tag{2.60}$$

Here,

κ_F = Relative strength of the driving term versus the island,
$\mathbf{f_v} \cdot \hat{z} = \kappa_F \Omega_{z,0} f(r)$
$g_0(r) = \int_0^r \frac{r'}{R_0} f(r') dr'$
$g(r) = \int_{r_{s+}}^r \frac{r'}{R_0} f(r') dr'$.

Using these forms of the profiles, the jumps in derivatives can readily be calculated. We find

$$\begin{aligned} \left[\mu r^3 \frac{\partial \Omega_\theta}{\partial r} \right]_{r_{s-}}^{r_{s+}} &= -\frac{\Omega_{\theta,0}}{\int_{r_{s+}}^a (\mu r^3)^{-1} dr}, \\ \left[\mu r \frac{\partial \Omega_z}{\partial r} \right]_{r_{s-}}^{r_{s+}} &= -\Omega_{z,0} \left\{ \frac{1}{\int_{r_{s+}}^a (\mu r)^{-1} dr} + \kappa_F \Big(\frac{\int_{r_{s+}}^a g(r') dr'/\mu r'}{\int_{r_{s+}}^a dr'/\mu r'} - g_0(r_{s-}) \Big) \right\}. \end{aligned} \tag{2.61}$$

Now the forces are found to be

$$\begin{aligned} T_{\theta,VS} &= -4\pi^2 R_0 \frac{\Omega_{\theta,0}}{\int_{r_{s+}}^a (\mu r^3)^{-1} dr}, \\ T_{z,VS} &= -4\pi^2 R_0^3 \Omega_{z,0} \left\{ \frac{1}{\int_{r_{s+}}^a (\mu r)^{-1} dr} + \kappa_F \Big(\frac{\int_{r_{s+}}^a g(r') dr'/\mu r'}{\int_{r_{s+}}^a dr'/\mu r'} - g_0(r_{s-}) \Big) \right\}. \end{aligned} \tag{2.62}$$

This concludes the calculation of the viscous forces.

2.2.5 Viscous drag and phase shifts

We now need to relate how the electromagnetic and viscous forces interact with the island. These interactions will give rise to a phase shift $\Delta\varphi$, and eddy currents. To investigate the specifics of this, we'll have to make use of the layer equations. These describe the dynamics of the plasma within a small layer surrounding the magnetic island. These are derived in Ara's 1978 paper [28]. We now give a brief overview of this derivation.

Layer equations

The two-fluid model will be used to derive this set of layer equations. We will write equations (2.18) in a slightly different form:

$$\begin{aligned}
&\frac{\partial n_\alpha}{\partial t} + \nabla \cdot (n_\alpha \mathbf{U}_\alpha) = 0, \\
&\frac{3}{2} n_\alpha \Big(\frac{\mathrm{D}T_\alpha}{\mathrm{D}t}\Big)_\alpha + p_\alpha \nabla \cdot \mathbf{U}_\alpha = 0, \\
&\frac{\partial \mathbf{B}}{\partial t} = -\nabla \times \mathbf{E}, \\
&\nabla \times \mathbf{B} = \mu_0 \mathbf{J}, \\
&\rho \Big(\frac{\mathrm{D}\mathbf{U}_i}{\mathrm{D}t}\Big)_i = -\nabla p + \mathbf{J} \times \mathbf{B} - \nabla \cdot \mathbf{\Pi}_i, \\
&\mathbf{E} + \mathbf{U}_e \times \mathbf{B} = \eta \mathbf{J} - \frac{\nabla p_e}{ne}
\end{aligned} \tag{2.63}$$

Here, α is now an index for the ion and electron species. We assume that all quantities only depend on the radial coordinate. Investigating the radial component of Ohm's law, and the ion momentum equation we find

$$\begin{aligned}
\frac{\partial p_e}{\partial r} &= \quad -ne(E_r + U_{e,\theta} B_z - U_{e,z} B_\theta), \\
\frac{\partial p_i}{\partial r} &= \qquad ne(E_r + U_{i,\theta} B_z - U_{i,z} B_\theta).
\end{aligned} \tag{2.64}$$

For the equilibrium quantities we assume that the ion flow is purely toroidal (thus axial in the cylinder). By relating the electron flow to the current we then find

$$\begin{aligned}
U_{i,z} &= \quad \frac{E_r}{B_\theta} - \frac{1}{B_\theta ne} \frac{\partial p_i}{\partial r}, \\
U_{i,\theta} &= \qquad\qquad 0, \\
U_{e,z} &= \qquad U_{i,z} - \frac{J_z}{ne}, \\
U_{e,\theta} &= -\frac{E_r}{B_z} - \frac{1}{B_z ne} \frac{\partial p_e}{\partial r}
\end{aligned} \tag{2.65}$$

The analysis will be continued in a frame of reference in which $E_r = 0$, thus with a velocity of E_r/B_θ in the toroidal direction. We linearize the momentum ion momentum equation and Fourier transform it to find

$$\begin{aligned}
-i\omega' \rho U_{i,r,1} = &- \frac{\partial}{\partial r}\Big[p_1 + \mathbf{B}_0 \cdot \mathbf{B}_1/\mu_0\Big] - 2\frac{B_{\theta,0} B_{\theta,1}}{\mu_0 r} + i\mathbf{k} \cdot \mathbf{B}_0 B_{r,1}/\mu_0 + \\
&\mu \frac{\partial^2}{\partial r^2} U_{i,r,1}, \\
-i\omega' \rho U_{i,\theta,1} = &- mi\Big[p_1 + \mathbf{B}_0 \cdot \mathbf{B}_1/\mu_0\Big]/r + \frac{B_{\theta,0} B_{r,1}}{\mu_0 r} + i\mathbf{k} \cdot \mathbf{B}_0 B_{\theta,1}/\mu_0 + \\
&\mu \frac{\partial^2}{\partial r^2} U_{i,\theta,1} + \frac{B_{r,1}}{\mu_0} \frac{\partial B_{\theta,0}}{\partial r},
\end{aligned} \tag{2.66}$$

where $\omega' = \omega - k_z E_r / B_{\theta,0}$, the Doppler shifted typical frequency, and $\mathrm{k} \cdot \mathrm{B}_0 \mathrm{m} \mathrm{B}_{\theta,0}/r + k_z B_{z,0}$. To derive the equations of (2.66), we have assumed that both the perturbed magnetic field and velocity field have no toroidal component. Furthermore, we assume that within the singular layer $\partial^2 f_1/\partial r^2 \gg f_1/r^2$. From these two equations we can derive that for $m = -1$ modes, the following holds:

$$\mu_0 \rho \Big(\omega' - i \frac{\mu}{\rho} \frac{\partial^2}{\partial r^2}\Big) \frac{\partial^2}{\partial r^2} U_{i,r,1} = -\mathbf{k} \cdot \mathbf{B}_0 \frac{\partial^2}{\partial r^2} B_{r,1}. \tag{2.67}$$

We relate this equation to a radial displacement by stating $\hat{\xi} \propto e^{-i\omega' t}$. This gives us

$$i\mu_0 \rho \omega' \Big(\omega' - i \frac{\mu}{\rho} \frac{\partial^2}{\partial r^2}\Big) \frac{\partial^2 \hat{\xi}}{\partial r^2} = \mathbf{k} \cdot \mathbf{B}_0 \frac{\partial^2}{\partial r^2} B_{r,1}. \tag{2.68}$$

From the linearized Ampere's law, one can find

$$B_{r,1} = i\mathbf{k} \cdot \mathbf{B}_0 \hat{\xi} + i \frac{\eta}{\mu_0 \omega'} \frac{\partial^2 B_{r,1}}{\partial r^2}. \tag{2.69}$$

We expand the last two equations about the resonant surface to find

$$\begin{aligned} i \frac{\partial^2 \psi}{\partial y^2} &= -\omega' \tau_R (\psi - y\phi), \\ y \frac{\partial^2 \psi}{\partial y^2} &= (\omega' \tau_A)^2 \frac{\partial^2 \phi}{\partial y^2} + i \frac{\omega' \tau_A^2}{\tau_V} \frac{\partial^4 \phi}{\partial y^4}. \end{aligned} \tag{2.70}$$

Here,

ψ = the perturbed poloidal flux,
$\phi = s(r_s) B_{\theta_0}(r_s) \hat{\xi}$,
$y = r/r_s$,
$\tau_A = R_0 \sqrt{\mu_0 \rho(r_s)}/B_z n s_s$,
$\tau_V = r_s^2 \rho(r_s)/\mu(r_s)$,
$\tau_R = \mu_0 r_s^2 \eta(r_s)$.

These are the layer equations for a two fluid model.

Visco-resistive regime

We are interested in the behaviour of the layer when both viscosity and resistivity are important, which is needed to relate the phase shift to the plasma velocity. In this case the inertial effects play no part in the plasma evolution. This is true whenever we can neglect the ω'^2 term in equation (2.70). To see when this holds, we assume the ordering $\tau_R \gg \tau_V \gg \tau_A$. Fitzpatrick states that this holds whenever [15]:

$$\omega' \ll \tau_V^{1/3} / \tau_A^{2/3} \tau_R^{2/3}. \tag{2.71}$$

So whenever ω' is less than the combination of these timescales, inertial effects are unimportant. Using this result, Fitzpatrick shows that

$$\Delta' r_s \approx 2.1036 i\omega' \Big(\frac{\tau_A^2 \tau_R^5}{\tau_V}\Big)^{1/6}. \tag{2.72}$$

Now we need to relate these expressions to the angle between the external perturbation and the tearing mode. Rearranging the Rutherford stability parameter of equation (2.36), we find,

$$\frac{\psi_k}{\Psi_{vac}} e^{i\Delta\varphi} = \frac{1}{1 - \Delta'/\Delta'_{mode}}, \tag{2.73}$$

where $\Psi_{vac} = -2m\psi_{vac}(r_k)/r_k\Delta'_{mode}$. Using this expression one can find that the angle reduces to

$$\Delta\varphi = \arctan\left(\frac{\mathrm{Im}(\Delta'/\Delta'_{mode})}{\mathrm{Re}(1 - \Delta'/\Delta'_{mode})}\right). \tag{2.74}$$

Filling in the known expression for Δ', one can find that

$$\sin(\Delta\varphi) = \frac{A\omega'}{\sqrt{1 + (A\omega')^2}}, \tag{2.75}$$

where $A = 2.1036\Big(\frac{\tau_A^2 \tau_R^5}{\tau_V}\Big)^{1/6} \frac{1}{\Delta'_{mode} r_s}$. This has the expected behaviour we expanded upon in the heuristic model, namely linear for low velocities, and converging to some asymptote for high velocities. Finally, we can also calculate the magnitude of ψ_k/Ψ_{vac}. This reduces to

$$\left|\frac{\psi_k}{\Psi_{vac}}\right| = \frac{1}{\sqrt{1 + (A\omega')^2}}. \tag{2.76}$$

This has the expected $1/\omega$ behaviour in the high velocity regime.

2.2.6 Mode penetration

We now bring everything together to derive the central equations describing mode penetration events. First, we remind ourselves of the form of the viscous force:

$$\begin{aligned} T_{\theta,VS} &= -C_{\theta,VS}\Omega_{\theta,0}, \\ T_{z,VS} &= -C_{z,VS}\Omega_{z,0}. \end{aligned} \tag{2.77}$$

Secondly, we recall the form of the electromagnetic force namely:

$$\begin{aligned} T_{\theta,EM} &= -4\pi^2 R_0 \frac{m^2}{\mu_0} \psi_k \psi_{vac}(r_{k+}) \sin\Delta\varphi, \\ T_{z,EM} &= -\frac{1}{q_s} T_{\theta,EM} \end{aligned} \tag{2.78}$$

Using all the results from the previous page, we find that the electromagnetic force reduces to the form

$$\begin{aligned} T_{\theta,EM} &= -C_{\theta,EM}\psi_{vac}^2 \frac{\omega'}{A+\omega'^2}, \\ T_{z,EM} &= -\frac{1}{q_s} T_{\theta,EM} \end{aligned} \tag{2.79}$$

Here $\omega' = m\Omega_\theta - n\Omega_z$, which can be interpreted as the non-helical part of the rotation (that is, perpendicular to the (m,n) magnetic field lines). To cast the viscous force into non-helical coordinates, we define

$$\omega_0 \equiv m\Omega_{\theta,0} - n\Omega_{z,0} \tag{2.80}$$

These are all the relevant equations. Please note the dependence of the different torques - viscous torques scale linearly with plasma velocity whereas electromagnetic torques scale linearly only for small velocities, and asymptotically grow to zero for high velocities. To find the steady state behaviour, we simply set forces the sum of torques to zero. However before we do so, we will introduce a novel component into our model. There might be an extra torque working on the islands, namely an external NBI-torque. We will take this to be some constant $T_{z,NBI}$, working only in the toroidal (or axial) direction. This reduces our full set of equations to.

$$\begin{aligned} T_{\theta,EM} + T_{\theta,VS} &= 0 \\ T_{z,EM} + T_{z,VS} + T_{z,NBI} &= 0 \end{aligned} \tag{2.81}$$

Let us go through the algebra. Substituting equation (2.80) in the first equation of (2.81) one finds,

$$T_{z,EM} = \frac{n}{m} T_{\theta,VS}.$$

Now the second equation of (2.81) reduces to

$$\frac{n}{m} T_{\theta,VS} + T_{z,VS} + T_{z,NBI} = 0.$$

We can solve this equation for $\Omega_{z,0}$, which gives us,

$$\Omega_{z,0} = \frac{1}{C_{z,VS}} \left[T_{z,NBI} - \frac{n}{m} C_{\theta,VS}\Omega_{\theta,0} \right].$$

We can use this expression to find the relationship between ω_0 and $\Omega_{\theta,0}$. This leaves us with

$$\Omega_{\theta,0} = \frac{\omega_0 - nT_{z,NBI}/C_{z,VS}}{m + n^2 C_{\theta,VS}/mC_{z,VS}}.$$

Now comes an important assumption. We assume that in steady state tearing mode will almost exactly follow the plasma velocity (as it will be viscously dragged

along by it, until the viscous forces are zero). Thus we can set $\omega_0 = \omega' - \Delta\omega$. We can then use the poloidal force equation (the first of equation (2.81) to find

$$C_{\theta,VS}\frac{nT_{z,NBI}/C_{z,VS} - \omega' + \Delta\omega}{m + n^2 C_{\theta,VS}/mC_{z,VS}} = C_{\theta,EM}\psi_{vac}^2\frac{\omega'}{A + \omega'^2}. \tag{2.82}$$

This in the exact form we want it in. On the LHS, we have no dependence on the perturbation strength and a linear dependence on plasma velocity, offset by some value. On the RHS we have a scaling quadratically in the perturbation strength, linear in plasma velocity for low velocities, and $1/\omega'$ for high plasma velocities. This is exactly as in the heuristic model.

Interestingly, the novel component $T_{z,NBI}$ acts as an offset. This has the consequence that increasing the NBI torque raises the critical field strength at which mode penetration occurs. Thus if one wants to operate at high error field strengths, one could ensure that mode penetration does not occur by increasing the NBI torque in the island region. This holds assuming that the other factors on the LHS of equation (2.82) are only weakly dependent on the NBI torque. If not, one could still use the dependence on $T_{z,NBI}$ to control the critical field strength.

2.3 Visco-resistive equilibria

To make sure we start our simulations in an equilibrium state (which we will then perturb in a manner consistent with mode-penetration), we need to calculate equilibrium states. In this section, we derive a set novel set of equations, describing a visco-resistive equilibrium. These equations will thus be used to initialize the M3D-C1 simulations. Firstly, we set out to find a list of equations which describe visco-resistive equilibria. The following set of assumptions are made.

1. Loop voltages drive toroidal currents
2. The plasma is heated both ohmically and via a source term (e.g. via ion cyclotron resonant heating)
3. Ion and electron temperatures are equal
4. The plasma loses thermal energy conductively
5. The plasma is in force balance
6. The source term driving plasma flow is purely toroidal
7. The total toroidal plasma current is constrained to a certain value
8. Magnetic fields and currents have no radial component
9. Spitzer resistivity holds
10. Viscoscity and heat diffusivity are arbitrary continuous functions of the minor radial coordinate

This corresponds to the following set of equations,

$$\begin{aligned}
\eta J_\phi = & \quad \frac{V_L}{2\pi R_0}, \\
\eta J_\phi^2 + P = & \quad -\nabla\cdot(\kappa\nabla T_e), \\
(\mathbf{J}\times\mathbf{B})\cdot\hat{r} = & \quad \nabla p\cdot\hat{r}, \\
(\nabla\cdot[\mu(\nabla\mathbf{u}+(\nabla\mathbf{u})^T)])\cdot\hat{\phi} = & \quad -\mathbf{f}\cdot\hat{\phi} \\
\int J_\phi da = & \quad I_p
\end{aligned} \tag{2.83}$$

where:

η = Spitzer resistivity,
$\mathbf{J}$ = Plasma current,
V_L = Loop voltage,
R_0 = The major radius,
P = The external heating source,
κ = The thermal conductivity,
T_e = The electron temperature,
$\mathbf{B}$ = The magnetic field,
p = The plasma pressure,
μ = The plasma viscoscity,
$\mathbf{u}$ = The plasma velocity,
$\mathbf{f}$ = The force density of the beam driving plasma flows,
I_p = The total plasma current.

It is important to note that all these variables, except for V_L, I_p and R_0, can be functions of the minor radial coordinate. In passing we note that using these assumptions, one can derive a set of scaling laws which have been included in the appendix. We solve for these equations one at a time, begin with the temperature equation.

Temperature equation

We start by squaring Ohm's law, or the first equation of (2.83), and substituting this in the temperature equation. Furthermore, the operators are written out in cylindrical geometry and the resistivity is substituted with its Spitzer form $\eta = \eta_0 T^{-3/2}$. This reduces the equation to the final form,

$$\Big[\frac{V_L}{2\pi R_0}\Big]^2 \frac{T(r)^{3/2}}{\eta_0} + P(r) = -\frac{1}{r}\frac{\partial[r\kappa(r)T'(r)]}{\partial r}. \tag{2.84}$$

Now we proceed to make the equation dimensionless. We split up the profiles into products in the following fashion:

$$\begin{aligned} r &= a\rho, \\ T(r) &= T_0 t(r), \\ \kappa(r) &= \kappa_0 k(r), \\ P(r) &= \beta\Big[\frac{V_L}{2\pi R_0}\Big]^2 \frac{T_0^{3/2}}{\eta_0} p_{heat}(r). \end{aligned} \tag{2.85}$$

Here,

a = The minor radius
T_0 = The central temperature
κ_0 = The central heat diffusivity
β = The fraction of ohmic heating that comes from an external source

This allows us to rewrite equation (2.84) in the following dimensionless form

$$\begin{aligned} \gamma[t(\rho)^{3/2} + \beta p_{heat}(\rho)] = & \quad -\frac{1}{\rho}\frac{\partial \rho k(\rho) t'(\rho)}{\partial \rho}, \\ \gamma = & \quad \frac{a^2 T_0^{1/2}}{\kappa_0 \eta_0}\Big(\frac{V_L}{2\pi R_0}\Big)^2. \end{aligned} \tag{2.86}$$

This is a second order ODE which needs to be solved for three different conditions:

$$t'(0) = 0, \qquad t(0) = 1, \qquad t(1) = t_{edge}. \tag{2.87}$$

Two of these conditions can be used as boundary conditions for the ODE, and the third one sets a value for γ. We are nearly in a position to calculate T_0, but not quite. V_L is another unknown in this system of equations, so we need to be able to relate these two to one and another before we can completely determine the temperature profile. This can be done after we have determined an expression for the magnetic field, which is done next.

Poloidal magnetic field equation

The poloidal magnetic field can easily be calculated from the toroidal current flowing through the plasma. This is because of Amperè's circuital law,

$$\oint_{\partial S} B_p(r)dl = \mu_0 \iint_S J_\phi dS \tag{2.88}$$

From ohm's law, an expression for the axial current is quite readily found. This is combined with equation (2.86) gives the following expression for the axial current,

$$J_\phi = \frac{V_L T_0^{3/2}}{2\pi R_0 \eta_0}\Big(\frac{1}{\gamma}\frac{1}{\rho}\frac{\partial[\rho k(\rho)t'(\rho)]}{\partial\rho} + \beta p(\rho)\Big). \tag{2.89}$$

Since the total current was defined to be I_p, we can integrate equation (2.89) over the entire area to find,

$$I_p = -\frac{a^2 V_L T_0^{3/2}}{R_0\eta_0}\Big(\frac{1}{\gamma}\int_0^1 \frac{1}{\rho}\frac{\partial[\rho k(\rho)t'(\rho)]}{\partial\rho}\rho d\rho + \beta\int_0^1 p_{heat}(\rho)\rho d\rho\Big). \tag{2.90}$$

Using the boundary conditions defined in (2.87), and defining the total integral of the heat deposition as p_{tot}, the final expression becomes

$$I_p = -\frac{a^2 V_L T_0^{3/2}}{R_0\eta_0}\Big(\frac{k(1)t'(1)}{\gamma} + \beta p_{tot}\Big). \tag{2.91}$$

From this equation, an important property for equilibria can already be deduced. Since I_p is positive definite, and it is reasonable to assume that the temperature is strictly decreasing near the edge, this equation can only hold if

$$0 \leqslant \beta < \Big|\frac{k(1)t'(1)}{\gamma p_{tot}}\Big|. \tag{2.92}$$

To interpret what this means, we use equations (2.86) and (2.91) to find the final temperature and loop voltages of the steady-state solution. Solving these two equations, one finds that

$$\begin{aligned} V_L &= \left[\frac{64\pi^6\eta_0^2\kappa_0^3 R_0^5}{a^4 I_p}(-\gamma)^2(k(1)t'(1)+\beta\gamma p_{tot})\right]^{1/5}, \\ T_0 &= \left[\frac{\eta_0^2 I_p^4}{16\pi^4 a^4\kappa_0^2}\frac{-\gamma^2}{(k(1)t'(1)+\beta\gamma p_{tot})^4}\right]^{1/5}. \end{aligned} \tag{2.93}$$

From equation (2.93) we can see that if a larger fraction of heating is supplied by a non-ohmic source, the central temperature increases rapidly. As ohmic heating scales as $\eta J^2 \propto V_L^2 T_0^{3/2} \propto (k(1)t'(1)+\beta\gamma p_{tot})^{-4/5}$, the amount of ohmic heating also increases. These two processes strengthen each other, and they diverge at a critical value where the temperature can grow indefinitely. Equation (2.92) shows what

this critical value is. This argument breaks down as efficiency of energy transfer is dependent on temperature as well. At high temperatures, less and less energy is transferred from the source to the plasma, so that these processes cannot strengthen each other indefinitely.

A second interesting caveat of equation (2.93) is the seemingly counter-intuitive results that for higher plasma currents, less loop voltage is needed. This can be understood as follows: there are two effects competing for the increase and decrease of loop voltage. The increasing effect is simply Ohm's law $V_L = \Omega I_p$. The decreasing effect is the temperature dependence of Spitzer resistivity (for higher temperatures, resistivity decreases). Since driving more current increases temperature via Ohmic heating, the temperature increases and resistivity decreases. In the end, the decreasing effect of the resistivity wins out over Ohm's law, giving rise to this counter-intuitive result.

We are now also in a position to calculate the poloidal magnetic field. We adjust the bounds of the integral of equation (2.90) to run from zero to some normalized radius ρ, and we substitute in the results from (2.93). Combining this with Amperè's circuital law, one finds that

$$B_p(\rho) = \frac{\mu_0 I_p}{2\pi a}\left[\frac{\beta\gamma\int_0^\rho \hat{\rho}p_{heat}(\hat{\rho})d\hat{\rho}/\rho + k(\rho)t'(\rho)}{\beta\gamma p_{tot} + k(1)t'(1)}\right]. \tag{2.94}$$

It is easily verified that at the edge, the poloidal magnetic field reduces to $\mu_0 I_p/2\pi a$. This is what one would expect from Amperè's circuital law. We further simplify equation (2.94) by referring to the term in square brackets as $b(\rho)$ and the prefactor as B_{max}, thus reducing the equation to

$$B_p = B_{max} b(\rho). \tag{2.95}$$

Pressure equation

The pressure can be found from the MHD force balance equation. Using $\mathbf{B} = B_\phi\hat{\phi} + B_p\hat{\theta}$, the MHD force balance reduces to

$$\frac{\partial p}{\partial r} = -\frac{1}{\mu_0}\left[\frac{1}{2}\frac{\partial B_p^2}{\partial r} + \frac{1}{2}\frac{\partial B_z^2}{\partial r} + \frac{B_p^2}{r}\right]. \tag{2.96}$$

We relate the toroidal magnetic field to the poloidal field via the q-profile,

$$B_z = \frac{R}{r}q(r)B_p. \tag{2.97}$$

We proceed to make the equation dimensionless in the following fashion:

$$\begin{aligned} p &= p_0\Pi(r) \\ \epsilon &= a/R_0. \end{aligned} \tag{2.98}$$

This leaves us with the following final equation for the pressure,

$$\begin{aligned}\frac{\partial \Pi}{\partial \rho}\beta_p &= -\Big[\frac{\partial b(\rho)^2}{\partial \rho} + \frac{1}{\epsilon^2}\frac{\partial [q(\rho)b(\rho)/\rho]^2}{\partial \rho} + 2\frac{b(\rho)^2}{\rho}\Big], \\ \beta_p &= \frac{2\mu_0 p_0}{B_{max}^2}.\end{aligned} \tag{2.99}$$

Equation (2.99) needs to be solved subject to two conditions,

$$\Pi(0) = 1, \qquad \Pi(1) = \Pi_{edge}. \tag{2.100}$$

One of these conditions can be used as a boundary condition to the ODE, and the other one can be used to set β_p. It is interesting to note that $\Pi'(0) = 0$, provided that $p_{heat}(r)$ does not diverge near the centre and that $q(r)$ is approximately constant to first order around the centre. This can easily be shown using L'Hôpital's rule. The condition ensures that the pressure profile is flat in the centre. Finally, we choose to add the option to impose a flat toroidal field profile. This leaves an extra degree of freedom, namely q_0. This can be chosen arbitrarily.

Velocity equation

The velocity equation can be quite readily obtained from equation (2.83). Writing out all the derivatives and dyads the scalar equation reduces to

$$\mu \frac{1}{r}\frac{\partial}{\partial r}\Big[r\frac{\partial v_\phi}{\partial r}\Big] + \frac{\partial \mu}{\partial r}\frac{\partial v_\phi}{\partial r} = -f_\phi. \tag{2.101}$$

We once more make use of the same recipe to make the equation dimensionless. We define the dimensionless profiles in the following manner,

$$\begin{aligned} v_\phi &= v_0 v(r), \\ \mu &= \mu_0 \text{מ}(r), \\ f_\phi &= f_0 f(r). \end{aligned} \tag{2.102}$$

This reduces the ODE to it's dimensionless form

$$\begin{aligned} \frac{\text{מ}}{\rho}\frac{\partial}{\partial \rho}[\rho v'] + \text{מ}' v' &= -\alpha f, \\ \alpha &= \frac{f_0 a^2}{\mu_0 v_0}. \end{aligned} \tag{2.103}$$

Equation (2.103) needs to be solved, subject to three boundary conditions,

$$v'(0) = 0, \qquad v(0) = 1, \qquad v(1) = 0. \tag{2.104}$$

Two can be used as boundary conditions for the second order ODE, and one can be used to set α.

Numerical implementation

Finally, we dedicate short section to clarify how these equations are solved numerically. As the problem comes down to solving second and first order ODEs, we clarify how an exemplary case is solved. Firstly, for first order ODEs the form of equation (2.99) is

$$f'(\rho) = \lambda g(\rho), \qquad f(0) = 1, \qquad f(1) = f_{end} \tag{2.105}$$

where:

$f(\rho) =$ The equation to be solved for
$g(\rho) =$ Some known function
$\lambda \quad =$ A parameter

Choosing some arbitrary value for λ, this can easily be solved using forward Euler

$$f_{n+1} = f_n + \Delta h \lambda g_n, \qquad f_0 = 1. \tag{2.106}$$

Here, the subscript n denotes the different node locations on which it is solved, and Δh is the step-size of the method. This however, does not solve our second boundary condition (unless we had a very lucky guess for λ). We do know that the final value of f using this method, is some function of λ. In other words, our condition can thus be stated as

$$f_{final}(\lambda) = f_{end}. \tag{2.107}$$

This is in essence a simple root finding problem. We solve this by making use of the Newton-Rhapson method. This can be best understood as a discrete Taylor expansion. Say $f_{final}(\lambda)$ has been sampled at λ_{i-2} and λ_{i-1}. The next guess, λ_i, will then uphold the equation

$$\begin{aligned} f_{final}(\lambda_i) \approx \quad & f_{final}(\lambda_{i-1}) + \frac{f_{final}(\lambda_{i-2}) - f_{final}(\lambda_{i-1})}{\lambda_{i-2} - \lambda_{i-1}}(\lambda_i - \lambda_{i-1}), \\ 0 = \quad & f_{final}(\lambda_{i-1}) + \frac{f_{final}(\lambda_{i-2}) - f_{final}(\lambda_{i-1})}{\lambda_{i-2} - \lambda_{i-1}}(\lambda_i - \lambda_{i-1}). \end{aligned} \tag{2.108}$$

The guess is iterated until the answer is within some tolerance of f_{end}.

The technique for second order ODEs is not much different. The form of equation (2.86) is

$$\begin{aligned} &\lambda[f^{3/2} + \beta p_{heat}] = -\left[\frac{gf'}{\rho} + g'f' + gf''\right], \\ &f(0) = 1, \qquad f'(0) = 0, \qquad f(1) = f_{end}. \end{aligned} \tag{2.109}$$

We first split this up into two coupled first order ODEs. This is done by setting $f' = u$. The equation can now be written as

$$\begin{aligned} &u' = -\frac{1}{g}\left[\lambda(f^{3/2} + \beta p_{heat}) + \frac{gu}{\rho} + g'u\right], \\ &f' = u. \end{aligned} \tag{2.110}$$

This can be solved using forward Euler as well,

$$\begin{aligned} &u_{n+1} = u_n - \frac{\Delta h}{g_n}\left[\lambda(f_n^{3/2} + \beta p_{heat,n}) + \frac{g_n u_n}{\rho_n} + g_n' u_n\right], \\ &f_{n+1} = f_n + \Delta h u_n. \end{aligned} \tag{2.111}$$

To avoid numerical evaluation of the $1/\rho$ term, the value of $f''(0)$ is evaluated using L'Hôpital's rule. Using boundary conditions, it can be found to be

$$f''(0) = -\frac{\lambda + \lambda\beta p_{heat}(0)}{2}. \tag{2.112}$$

Again we find that f_{final} is a function of λ. We thus solve for the last boundary condition using the Newton-Rhapson method. The last second order ODE, equation (2.103) is solved in the same fashion.

It is important to note that the Newton-Rhapson method finds a solution, but it does not have to be a unique solution. To make progress, we simply assume uniqueness. This assumption is checked by verifying that the final profiles look physical. For all tests performed, this seems to be the case. This of course does not prove uniqueness, but it is a solid check to see if the found solution is sensible.

Code

A code calculating the different profiles using the previously mentioned numerical methods has been developed in fortran. It is made available online via GitHub under a MIT licence [29]. It comes with a fortran namelist as an input file for ease of use. Functions such as the heat diffusivity profile, need to be changed in the source code itself.

3 Benchmark & M3D-C1

3.1 Benchmark specification

Many benchmark options are available, but we choose one most similar to our case of interest. Q. Yu et al. have done work on error-field penetration with the initial-value code TM1 [16]. In this calculation, a cylindrical plasma column with parameters similar to the TEXTOR tokamak [30] (such as number density, plasma current, plasma temperature, minor radius, and more) is perturbed with a resonant magnetic perturbation (RMP) giving rise to islands and finally an error-field penetrated state. The fact that the simulations show a mode-penetration event is verified by investigating two cases. In one case, the initial plasma velocity on axis (and thus the momentum drive on-axis) is relatively low. In this case the critical field strength needed to achieve an error-field penetrated state is reached, and mode penetration is observed. In the second case the initial plasma velocity on axis (and thus the momentum drive) is relatively high. This in turn leads to a higher critical field strength, which is not exceeded. Now the plasma does not become mode penetrated. Both can be seen in figure 3.1. The effect of mode-penetration is readily seen in the graph plotting the island width over time, and in the plot of plasma velocity. The island width for the mode penetrated state grows to quite significant values (the solid line), whereas the case with no mode penetration stays small (the dotted line). For the plasma velocities, the mode penetrated state shows a clear halt of plasma velocity near the resonant surface (the solid line with low plasma velocity). The case without mode penetration is virtually unaffected (the solid line with high plasma velocity). There are some initial oscillations though, which are a result of the simulations relaxing towards equilibrium.

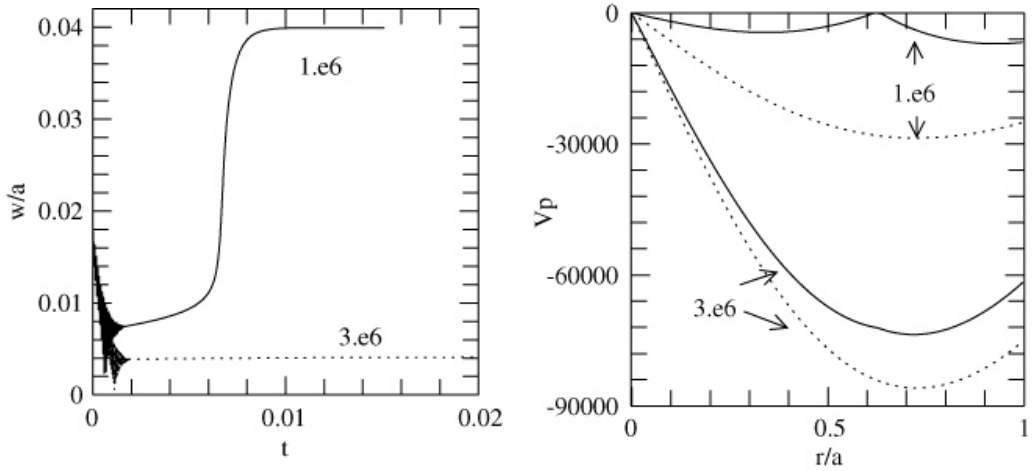

(a) Island width

(b) Poloidal plasma velocity

Figure 3.1: In figure 3.1a we see a plot of the island width as a function of time. On the y-axis, w/a denotes the normalized island width (fraction of minor radius). The x-axis is normalised with respect to resistive time-scales. After some initial oscillations the island width either blows up for a mode penetrated state (solid line), or stays small and is not mode penetrated (dotted line). In figure 3.1b, we see a plot of the poloidal plasma velocity for a mode-penetrated state, and a non-mode penetrated state. The mode penetrated state shows a clear decrease of plasma velocity on the resonant surface (the solid line with low velocities). The case with no mode-penetration shows no such behaviour (solid dotted line with higher plasma velocity). These graphs are taken from results obtained by Q. Yu et al. [16].

There are a few ways in which the research done by Q. Yu et al. differs from what is implemented in M3D-C1. Firstly, the force profile to drive plasma flows used in the benchmark case has a non-zero component at the location of the magnetic island. This means that they might not have observed mode penetration in a colloquial sense, but with the influence of external forcing (as presented in the theory section). Furthermore, the initial profiles for temperature and density in the benchmark are chosen (quite arbitrarily) to be parabolic. Finally, since only two parts of the parameter space have been sampled in the benchmark case, we cannot be sure that this is a mode-penetration event. A true mode penetration event is characterized by a sudden halt in plasma velocity (and correspondingly an island growth) when a critical field strength is exceeded. With only the two points there could be a continuous spectrum of island widths for different values of error field strength, without mode penetration ever occurring.
In M3D-C1 we choose to use a peaked force density profile, which has negligible strength near the magnetic islands. The initial profiles are calculated via the visco-resistive equilibrium equations, so that they should be in equilibrium.

3.2 Computational domain

We shortly clarify the different geometries and imposed coordinate systems used in the M3D-C1 simulations. The simulations are run in a cylindrical geometry, with periodic boundary conditions in the toroidal (or axial) direction. This is shown in figure 3.2. This differs from the true toroidal geometry, as we neglect curvature effects in the simulation (i.e., effects arising due to the curvi-linear coordinate system). We

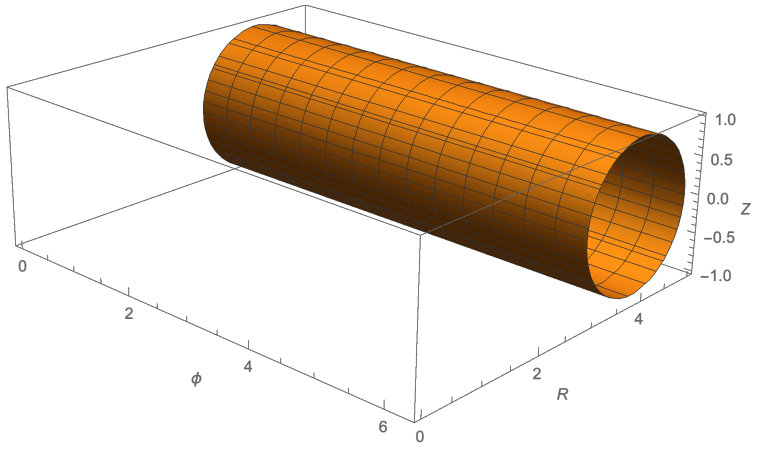

Figure 3.2: The geometry used for simulations in M3D-C1. The coordinate grid consists of Cartesian coordinates labelled by (R, Z, ϕ), where R corresponds to the major radial coordinate, Z corresponds to the vertical offset, and ϕ corresponds to the toroidal angle. The toroidal angle ϕ has a periodic boundary condition such that $f(R, Z, \phi = 0) = f(R, Z, \phi = 2\pi)$, for any function in this domain. A plasma column with minor radius 1 and major radius 4 can be seen in orange.

often convert this coordinate grid to cylindrical coordinates. Here we take the centre of the cylindrical plasma column at $\phi = 0$ to be the origin. Quantitatively the conversion between these two coordinate grids is as follows,

$$\begin{aligned} r &= \sqrt{(R - R_0)^2 + Z^2}, \\ \theta &= \arctan \frac{Z}{R - R_0}, \\ z &= R_0 \phi. \end{aligned} \tag{3.1}$$

Here, R_0 is the major radial coordinate. The periodicity of the toroidal coordinate implies that $f(r, \theta, z = 0) = f(r, \theta, z = 2\pi R_0)$.

3.3 Setting the parameters

It is important that the simulations in M3D-C1 are in similar parts of parameter space as compared to the research by Yu et al., to ensure that we are in physically similar regimes. The benchmark uses the following parameters:

$$\begin{aligned} T(r=0) &= 1800\ \mathrm{eV} \\ T(r=a) &= 300\ \mathrm{eV} \\ n_e(r=0) &= 3.2\cdot 10^{19}\ \mathrm{m}^{-3} \\ n_e(r=a) &= 3.0\cdot 10^{18}\ \mathrm{m}^{-3} \\ B_z(r=0) &= 2.5\ \mathrm{T} \\ q(r=0.6a) &= 2 \\ a &= 0.47\ \mathrm{m} \\ R &= 1.75\ \mathrm{m} \\ \tau_R &= a^2\mu_0/\eta \\ \chi_\perp &= 21a^2/\tau_R \\ \mu &= 21a^2/\tau_R \end{aligned} \tag{3.2}$$

Since the form of the resistivity is nowhere explicitly specified in the paper by Yu et al., we assume it to be Spitzer resistivity. The total plasma current is stated nowhere as well. Since we know it is based on TEXTOR-relevant parameters, we choose a typical value found in TEXTOR namely roughly 0.2 mega-Amperes [30–32]. We set the equilibrium equations and obtain the following values for physical parameters:

$$\begin{aligned} T(r=0) &= 920\ \mathrm{eV} \\ T(r=a) &= 128\ \mathrm{eV} \\ n_e(r=0) &= 3.6\cdot 10^{19}\ \mathrm{m}^{-3} \\ n_e(r=a) &= 3.2\cdot 10^{18}\ \mathrm{m}^{-3} \\ B_z(r=0) &= 2.78\ \mathrm{T} \\ q(r=0.5a) &= 2 \\ a &= 0.47\ \mathrm{m} \\ R &= 4.0\ \mathrm{m} \\ \tau_R &= 0.4\ \mathrm{s} \\ \tau_\chi &= 0.02\ \mathrm{s} \\ \tau_\mu &= 0.02\ \mathrm{s} \\ I_p &= 0.2\ \mathrm{MA} \end{aligned} \tag{3.3}$$

The profile shapes, after they have been imported to M3D-C1 can be seen below. These are the profiles that M3D-C1 will evolve. For completeness we also include the FORTRAN input file used for the equilibrium equations. It can be found in the appendix.

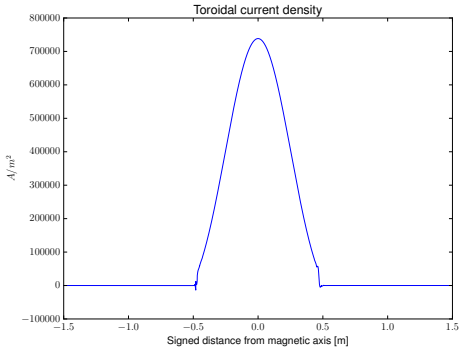

(a) The current density profile in the axial (or toroidal) direction.

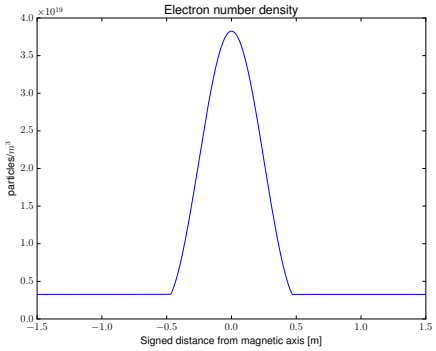

(b) The profile of the electron number density

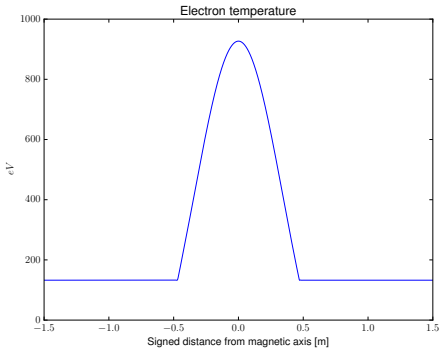

(c) The profile of the electron plasma temperature

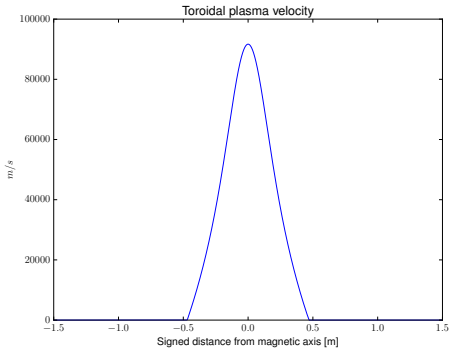

(d) The axial or toroidal component of the plasma velocity

Figure 3.3: The equilibrium profiles after they have been imported into M3D-C1. Signed distance measures the distance away from the magnetic axis, with positive being towards the outboard side and negative being towards the inboard side. The slight oscillations that can be seen at the edges of the current density profile are interpolation errors, and they fade away quite quickly as the profiles are evolved.

3.4 Numerical methods employed by M3D-C1

We take a section to briefly clarify the working principles of M3D-C1. M3D-C1 is a finite element method (FEM) code, which means it uses FEM to solve the set of partial differential equations described in equation (2.18). FEM approximates the true solution of the set of partial differential equations in the following manner. Let $u(x,t)$ be the solution to some differential equation. We set

$$u(x,t) \approx \sum_i u_i(t)\psi_i(x), \tag{3.4}$$

where $\psi_i(x)$ is a so-called basis function, u_i is the value of the function at a pre-described discrete node (node i). The basis function $\psi_i(x)$ takes on the value 1 at node i but is zero at every other node. There's a lot of freedom in chosing the basis function, but M3D-C1 chooses to use C^1 continuous basis functions which means that the basis function and its first derivative is continuous. To see how this approximation facilitates solving the partial differential equation, we look at the diffusion equation as an example,

$$\frac{\partial u}{\partial t} = \frac{\partial^2 u}{\partial x^2}. \tag{3.5}$$

We multiply this equation by some set of test-functions $\phi_j(x)$ and integrate over the entire domain Ω. This does mean that we implicitly assume that both the solution and the test function are members of Hilbert space, an assumption that is rarely broken.

$$\begin{aligned} \int_\Omega \frac{\partial u}{\partial t}\phi_j dx &= \int_\Omega \frac{\partial^2 u}{\partial x^2}\phi_j dx, \\ \int_\Omega \frac{\partial u}{\partial t}\phi_j dx &= \left[\phi_j \frac{\partial u}{\partial x}\right]_{\partial\Omega} - \int_\Omega \phi_j' \frac{\partial u}{\partial x} dx. \end{aligned} \tag{3.6}$$

We now take our test functions to be the same as our basis function. Note that this is not necessary, and one could in principle use different test and basis functions. We also substitute equation (3.4) as the solution to the PDE. We find

$$\sum_{i,j} u_i'(t) \int_\Omega \psi_i(x)\psi_j(x)dx = \sum_{i,j} \left[u_i(t)\psi_i'(x)\psi_j(x)\right]_{\partial\Omega} - \sum_{i,j} u_i(t) \int_\Omega \psi_j'(x)\psi_i'(x)dx. \tag{3.7}$$

Once boundary conditions are imposed, the system reduces to something of the form

$$\mathbf{M}\cdot\mathbf{u}'(t) = \mathbf{A}\cdot\mathbf{u}(t), \tag{3.8}$$

where $\mathbf{M}$ is often referred to as the mass-matrix, and $\mathbf{A}$ is often called the stiffness-matrix, and $\mathbf{u}$ is a vector with components u_i. The system has thus reduced to a simple system of first-order ODEs, which can be solved using a method of choice (e.g., Crank–Nicolson, Runga-Kutta, etc.). This example is meant to illustrate how using FEM we can convert some complicated differential equation with a solution that resides in function space, to first a discrete set equations using the test-functions, and finally to a vector equation using the basis functions. There are a lot more nuances and subtleties to how M3D-C1 employs FEM, which are clarified in a host of different papers [33–35].

3.5 M3D-C1 specifications

M3D-C1 can be run in a plethora of different configurations, so it is important to specify how we are exactly using M3D-C1. We highlight the most important of these settings. The full settings (which are specified in a FORTRAN namelist) can be found in the appendix. We run M3D-C1 in the following configuration:

- We use a one-fluid model (ion and electron fluids have the same velocities). This does not change the specifics of mode penetration significantly [16].
- The plasma current is held constant by applying a PID controller to the loop voltage (which drives plasma current). Quantitatively, the loop voltage is set by the following integro-differential equation

$$V_L(t) = Pe(t) + I\int_0^t e(\tau)d\tau + D\frac{\partial e(t)}{\partial t}, \tag{3.9}$$

  where $e(t)$ is the difference between the desired plasma current I_p and the measured one $I_p(t)$ ($e(t) = I_p(t) - I_p$). The P, I, and D terms are the same constants for all simulations.
- Resistivity is assumed to be of the Spitzer form, with a slight offset to avoid division by zero errors
- Viscosity is assumed constant over the entire plasma region
- Heat diffusivity is assumed constant over the entire plasma region
- We use 8 toroidal planes
- The mesh is an unstructured mesh, with a circular boundary
- We use a multi-domain set-up, with a plasma region, a conducting wall, and a vacuum region
- We run it in non-linear mode (as is essential for mode-penetration)
- We run it in straight tokamak (cylinder) mode

The mesh (the nodes of the basis functions) can be seen in the figure below.

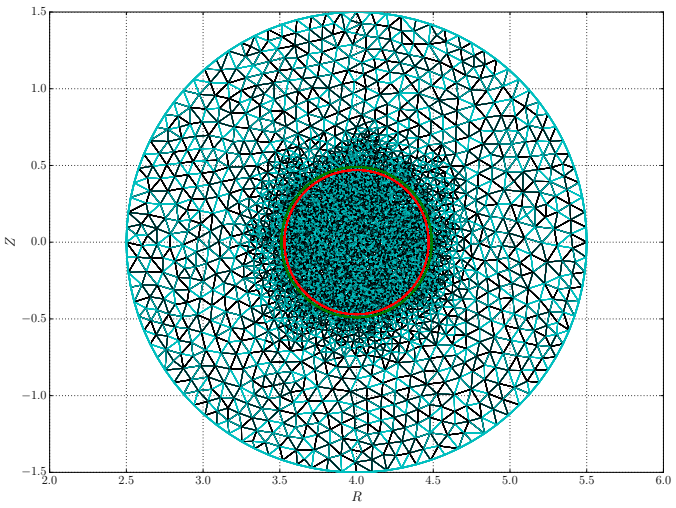

Figure 3.4: The mesh used in all simulations. This unstructured mesh has three different regions separated by colored circles; a plasma region, a wall region, and a vacuum region. These can be seen respectively as the centre circle, the inner annulus, and the outer annulus. The mesh is fine in the plasma region to properly resolve the islands, and is coarse in the vacuum region to speed up simulations.

3.6 Case specification

Three different cases have been simulated, which are meant to closely resemble the benchmark cases. We have one case where there is no NBI driving plasma flows. This case should feel no effect from the electromagnetic force, and should show a clear increase in magnetic island width. The second case has some NBI force driving plasma flows. This case should still be mode-penetrated (corresponding to the big-island case of the benchmark). The last case is one where there are strong plasma flows driven by NBI. This should correspond to the case where mode-penetration has not occurred in the research by Yu et al.. The NBI-profiles are all Gaussians, which are very peaked on axis (to avoid NBI-induced mode penetration). We quantify the respective NBI strengths by the central equilibrium plasma velocity as found by the visco-resistive equilibrium equations. The specific values can be found in the table below. Besides this the cases are all started with the same parameters. However, during the simulations various parameters were tweaked to circumvent numerical crashes (e.g. current hyperdiffusivity, number density diffusivity, wall resistivity). These were tweaked as little as possible, but still make for slightly different input files at the end of the simulations. This makes true benchmarking hard, as we stray from the original input parameters a bit.

Case 1	$v_0 = 0.0 \cdot 10^0$ m/s
Case 2	$v_0 = 9.2 \cdot 10^4$ m/s
Case 3	$v_0 = 1.8 \cdot 10^5$ m/s

Table 1: The central equilibrium velocity for each of the different cases.

4 Results

We show all relevant results obtained by M3D-C1 simulations in this section. A novel set of data acquisition and plotting routines used for these results were developed in an object oriented way for python. The structure of this plotting and data acquisition is highlighted in the appendix, and is made available on the M3D-C1 github.

4.1 Island width evolution

Using routines described in the appendix A.4, we can plot the island width as a function of time for the different cases tried in M3D-C1. This is shown in figure 4.1.

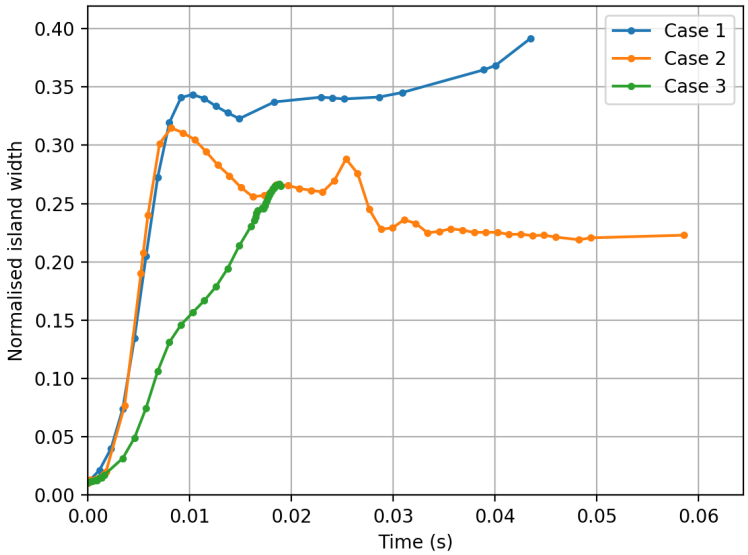

Figure 4.1: Island width as a function of time. Normalized island width denotes the island width w over the minor radius (i.e. w/a). Case 1 (no initial driving of flows) blows up to large island sizes, and M3D-C1 eventually crashes for this case. Case 2 (intermediate driving of flows) converges to some fixed island width, after some transients. Interestingly, the initial growth for case 1 and and case 2 is nearly identical, and only after this initial (linear) growth do differences occur. This is a strong indication that the non-linear island evolution is velocity dependent. This is again confirmed in case 3 (strong driving of plasma flows), which even shows a different initial growth in the linear regime. In the non-linear regime some small some differences can still be seen, but it is hard to tell as the simulation has not reached equilibrium. Case 3 has not converged, as M3D-C1 would crash at the latest time-step. This issue has not been resolved yet.

There are some important differences between the M3D-C1 results and the benchmark, the most obvious one being the quantitative difference between the island

sizes (which differ by an order of magnitude). Furthermore, we do not see similar trends for the island widths as seen in the research by Yu et al, indicating that we are not observing mode-penetration. The most likely reason for this will be expanded on in section 4.4. The results are interesting nonetheless, as they do show non-linear dependence of island width on plasma velocity. Most notably, the initial (linear) growth follows very similar patterns for all cases. However, after this initial growth, non-linear effects begin to dominate and differences between the cases becomes more pronounced. Case 1 (no driving of plasma flows) shows a growth of the island width in the non-linear phase, whereas case 2 and 3 do show a suppression of island width as compared to case 1. However, one should be careful in stating this for case 3 (with strong driving of plasma flows) as this case has not converged to equilibrium yet, so we do not know if the final state will be suppressed.

4.2 Island migration

Another interesting feature of the magnetic islands is that the X-points (the location where the separatrix becomes degenerate) tend to migrate inwards during the simulations, a novel observation. This can be seen in figure 4.2. The most likely cul-

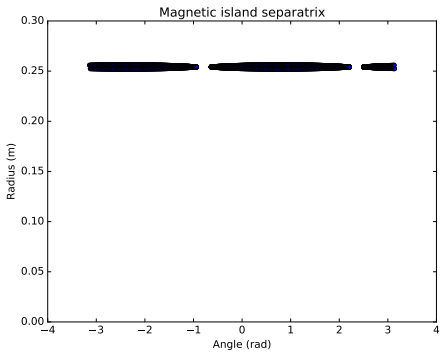

(a) Island at $t = 0$

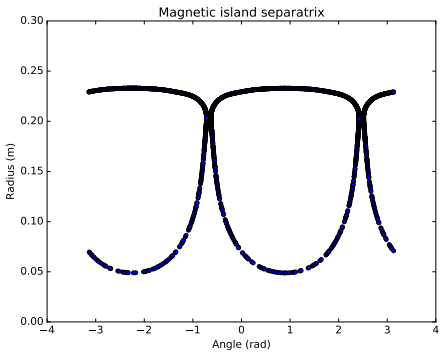

(b) Island at last time-step of case 1

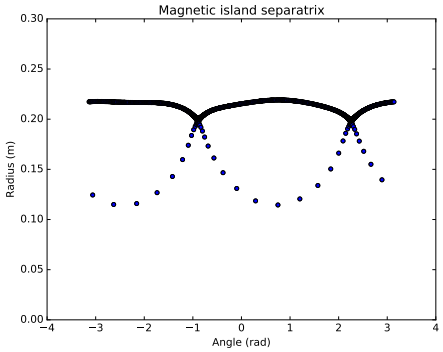

(c) Island at last time-step of case 2

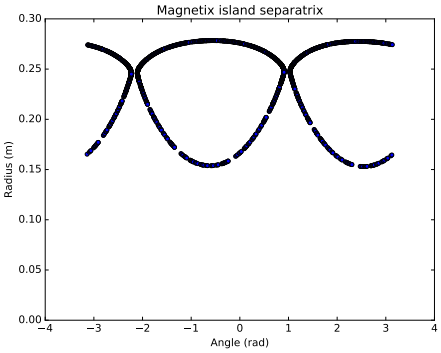

(d) Island at last time-step of case 3

Figure 4.2: The magnetic island separatrix for different simulations. Figure 4.2a shows the initial island separatrix at $t = 0$, which is the same for all simulations. Figure 4.2b shows the island separatrix at the last time-step for case 1. The island has significantly increased in size, and has shifted inwards (i.e. to smaller radial values). Figure 4.2c shows the island separatrix for the last time-step in case 2. This shows a similar behaviour as case 1; the island has shifted inward, and has increased in size. The increase in size however is less significant then in case 1. In interesting feature of this plot is that the underside of the separatrix is sampled much more sparsely than the upper half. This is most likely due to the fact that the original field line was just above the seperatrix, but accumulated errors eventually pushed the integrator to a new field line below the separatrix. Figure 4.2d shows the last time-step of case 3. This does show a clear increase in island size again, however the inward shift is much less pronounced. This is most likely due to the fact that this case was halted earlier than other cases.

prit for this inward shift is a change in the current density profile. We present the following novel explanation for this migration, exemplified in figure 4.3. We observe that the presence of the magnetic island tends to flatten out the current in the region of the magnetic island in the simulation. We postulate that this is most likely

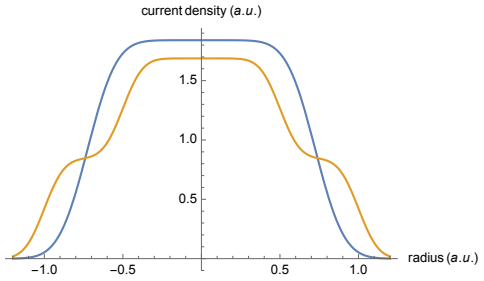

Figure 4.3: A sketch of the current density profile before the island has flattened the current (blue), and afterwards (orange). The magnetic island region resides $|r| \in [0.7, 0.9]$. Both current density profiles are calculated have the same amount of current running through them (i.e. $\int rj(r)dr$ is the same). This has the effect that the current density on axis is decreased.

due to enhanced transport within the magnetic island, but the mechanisms are not fully understood. Now, since there is feedback control (PID, via the loop voltage) on the total amount of current, the integral of the current density is conserved. The combination of the flattening of current density in the island region and the total current conservation has the effect that the central current density is decreased.

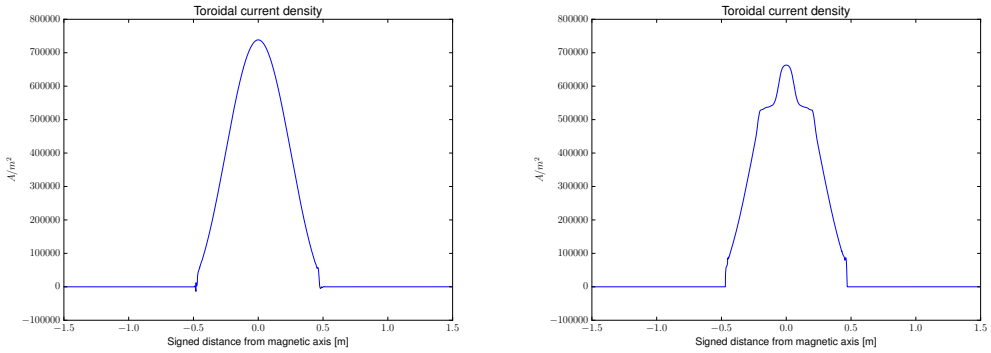

(a) Initial profile

(b) Final profile

Figure 4.4: Here we see a comparison of the toroidal current density profiles at the start and end of the simulation corresponding to case 1. The plots are toroidally averaged, to average out non-symmetric effects. We see the effects which were postulated; flattening of current density in island region, and decrease of central current density. The other cases show the same effects.

The central decrease is most likely a consequence of the cylindrical coordinate system. Namely, an increase of current density at larger r values weighs more heavily than a decrease at lower values (this is due to the extra r factor in the integral, arising from the Jacobian of the coordinate change). The decrease in turn effects the safety factor in the following manner. The central safety factor value q_0 can be

calculated as follows:

$$\begin{aligned} \lim_{r\to 0} B_p(r) &= \frac{\mu_0 \int j(r) r dr}{r} \approx \frac{\mu_0 \int j_0 r dr}{r} \quad = \frac{1}{2}\mu_0 j_0 r, \\ q_0 &= \lim_{r\to 0} \frac{r B_z}{R B_p(r)} = \frac{2B_z}{R\mu_0 j_0}. \end{aligned} \tag{4.1}$$

Thus we find that this decrease in central current density leads to an increase of the central safety factor. We also know that the edge safety factor is constant, since q_a is completely determined by the poloidal field at the edge ($B_p(a)$), which in turn is set by the total plasma current. Connecting q_0 and q_a in a similar way for the two profiles, we find that the r_s value where $q(r_s) = 2$ must shift inward. This is important as this $q = 2$ surface is the resonant surface on which this island resides. This decrease of j_0 is indeed also observed in the simulations. This is shown in figure 4.4. The inward movement is relevant, as it pushes the core structure into a more and more eccentric shape. If this eccentricity becomes too high reconnection might occur, changing the topology and transport near this essential core region.

4.3 Velocity profiles

One of the hallmarks of mode penetration events is the sudden decrease of plasma velocity near the resonant surface, which is also seen in figure 3.1. We check if a similar behaviour occurs for the three cases set up in M3D-C1. We define the positive poloidal plasma velocity as anti-clockwise rotating plasma. We obtain the graphs showcased in figure 4.5. One clear difference between the case by Yu et al.

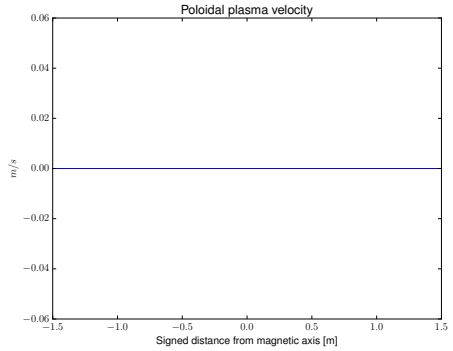

(a) Velocity at $t = 0$

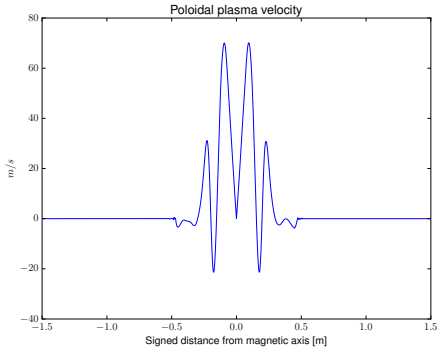

(b) Velocity at last time-step of case 1

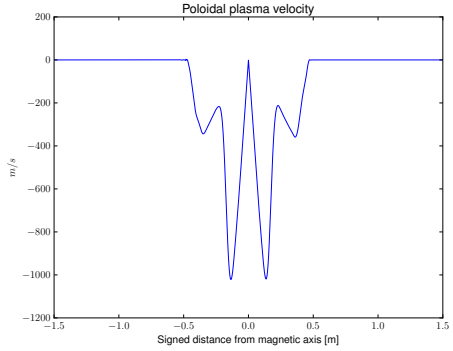

(c) Velocity at last time-step of case 2

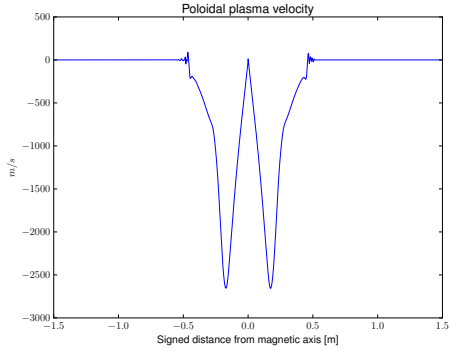

(d) Velocity at last time-step of case 3

Figure 4.5: The poloidal velocity profile for different simulations. Figure 4.5a shows the initial island poloidal velocity profile at $t = 0$, which is the same for all simulations. Figure 4.5b shows the poloidal velocity profile at the last time step of case 1. The velocity or comparatively small, and do not show a clear structure as in mode penetration. Figure 4.5c showcases the poloidal velocity at the last time step of case 2. Here we do see a pattern similar to that of a mode penetrated state: a clear reduction of plasma velocity near the resonant surface. However, the quantitative differences between this case and the benchmark are large. In figure 4.5d, we see the poloidal velocity profile at the last time step of case 3. The profile is much less comparable to that of the benchmark, but this could be because the simulation has not yet reached equilibrium.

and these cases is the quantitative difference in the poloidal plasma velocity. Yu had found poloidal plasma velocities of 10^4, roughly an order of magnitude higher than what was found in these simulations. One of the reasons that is stays much lower in these simulations is perhaps the large island obstructing it from flowing

any faster. We also attempted new simulations with higher driving of plasma flows. These became numerically stable quite quickly. This instability is most likely due to the fact that velocities become so high that they are comparable to Alfvénic velocites, and could be driving Alfvénic waves (meaning that time-steps have to be small enough to resolve Alfvénic responses and mesh has to be fine enough to resolve these waves). Toroidal velocities were observed to be roughly 10^5 meters per second in the simulations from M3D-C1. The central Alfvénic velocity can be found to be

$$\frac{B_z(0)}{\mu_0 \rho(0)} = 1.0 \cdot 10^7 \ m/s.$$

Here, ρ is the mass density. If one increases the toroidal velocities to be an order of magnitude higher, we see that we are already at 10% of the Alfvén velocity. Moreover, we are also at 1% of the speed of light. Although this is not a large fraction yet, some relativistic effects like synchrotron radiation might become more important sinks of energy.

4.4 Inherent stability

The most likely reason for the stark difference for the results by Yu et al. and the M3D-C1 case is the inherent differences of the tearing mode, arising from the Rutherford stability parameter as expanded on in section 2.2.2. In the 2008 paper it is stated that the mode is stable (meaning that it does not grow exponentially in the linearized theory). We however find different results when doing a run without a resonant magnetic perturbation, and with some small initial noise added. The mode does grow without bound in the linear version of M3D-C1. The mode structure, and the unbounded growth of the mode is shown in figure 4.6b. This growth of the tearing mode leads to the growth of the magnetic island, as the strength of the tearing mode is related to the island width via $W \propto \sqrt{\psi}$, as explained in section 2.2.2. Since the dominant response of the mode comes not from this external interaction with the perturbation but internally, we are not observing mode-locking. Stability was

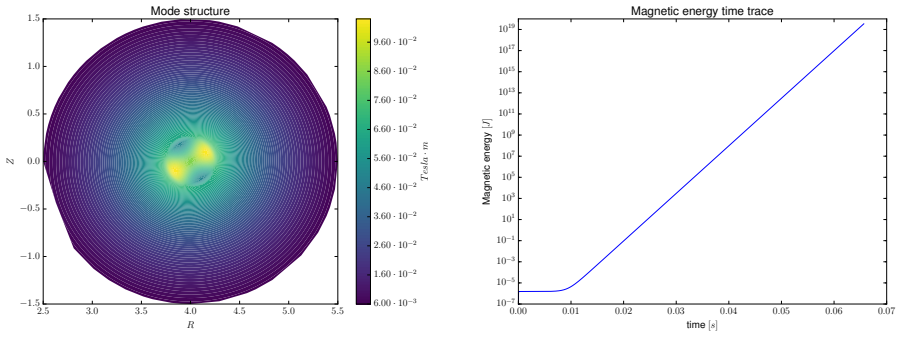

(a) Mode structure (b) Magnetic energy

Figure 4.6: In this figure we investigate the blow-up of the mode in the linearized version of M3D-C1. In figure 4.6a we plot the toroidal component of the vector potential $\mathbf{A}$ at $t = 0.03\ s$, where $\nabla \times \mathbf{A} = \mathbf{B}$. This shows a (2,1) mode structure. An even more telling sign that this is an unstable mode is the exponential blow up of the magnetic energy in figure 4.6b, which translates to a straight line on a log-plot.

also checked for various slightly differing cases (i.e. double the plasma current, half the major radius, etc.), but these were all found to be unstable. The stability difference might be different due to several reasons. Firstly, the stability could be very sensitive to equilibrium profiles, meaning that the differences between the visco-resistive equilibrium equations and the parabolic initial profiles assumed in the paper by Yu et al. could be enough to go beyond some stability threshold. Finally, although not stated in the paper, TM1 does have the option to add neo-classical terms (i.e. curvature terms) to the cylindrical MHD equations. These can have a stabilizing effects on the mode. These could perhaps be responsible for the mismatch as well. A proper check to find the reason for the mismatch would be to use initial profiles used in the paper by Yu in M3D-C1 as well, and check if they do show stability. Another option would be to check the stability of the visco-resistive solutions in TM1 to see if they differ from what has been found in M3D-C1.

5 Discussion

We find large discrepancies between the benchmark case and the M3D-C1 simulations, the first of which is the quantitative and qualitative difference in the island width for the varying cases. The most important contributor to this is the fact that the mode is unstable in M3D-C1, whereas in TM1 (the case tried by Yu et al.) it is stable. Some other reasons for this discrepancy in island width could be attributed to a host of different reasons. One reason might be that in the bench-mark case one is not observing mode-penetration in the colloquial sense, but mode penetration induced by force near the magnetic island (as explained in the theory section). Another possible culprit could be convergence of the M3D-C1, or the benchmark case. It has not been investigated that results stay the same for increasing mesh resolution, and temporal resolution. To ensure that this is no issue, a convergence study is needed. This would however be costly in terms of computation time needed (within the scope of this thesis), as the simulations presented here take roughly 2-3 weeks to finish per simulation. Since these were run on 16 nodes with 16 CPUs each, this is equivalent to roughly $16 \times 16 \times 2/52 \approx 10\ \mathrm{CPUYears}$.

The second interesting find is the migration of the island. Although no quantitative results are given of this in the benchmark paper, the island does seem to stay in its original position ($r = 0.6a$) in graphs presented (for example in figure 3.1). The mismatch could be explained by the large differences in island width. Islands were observed to have a flattening effect on the current density in the simulations done in M3D-C1. As these island become larger, the flattening effect takes place over a wider region. As explained, this reduces the central current density, and changes the q profile. As the islands in the benchmark case are much smaller, the flattening effect could have little to no effect on the central current density (and even the current density profile as a whole). This in turn ensures that the q profile is unchanged and island will stay in their original position.

The third discrepancy found is the difference in the poloidal plasma velocity profiles. Firstly, the quantitative difference is stark with the M3D-C1 case being roughly an order of magnitude lower than the benchmark case. Cases were tried with higher driving forces for plasma velocity, but these quickly became unstable. The reason for the mismatch is most likely again due to the stability of the mode. The islands are much larger in the M3D-C1 case, and since the island could be modelled as a solid body much more force is needed to accelerate the island. This is turn could lead to lower velocities of the plasma. Another possible reason is the closure chosen for the viscosity in M3D-C1. We choose it to be constant in the entire computational domain, but one could also use the Braginskii form of viscosity, or some other functional form. If this decreases the viscosity significantly (roughly an order of magnitude), then the discrepancy could be attributed to this fact. A final possible reason could be the model of the driving forces used. In M3D-C1 the driving forces are modelled as an NBI-injection. If the benchmark case uses a different model it could affect how strongly plasma flows are driven.

As pointed out in the previous paragraph, the most important reason for the differences is the inherent stability of the mode. It is found that the mode is unstable in the linear code version of M3D-C1, but stable in the benchmark case. The reason

for this is harder to pin-point, but we point out a multitude of possible reasons. Firstly, the initialisation of the codes was similar but not exactly the same for the codes. These slight differences could be enough to push M3D-C1 into an unstable regime, whereas TM1 stays within stability boundaries. To properly check this one could check the profiles used in M3D-C1 in TM1 for stability, and one could initialize M3D-C1 with the profiles used in TM1 to see if those are stable. Secondly, TM1 has a non-zero contribution of external driving force on the magnetic island. This in turn could effect stability, and even the physics of mode-penetration (as presented in the theory section). Thirdly, TM1 is a spectral code (meaning that it operates in Fourier space as opposed to real space) and truncation of these harmonics could affect stability properties of this mode. A convergence study would be required to verify that this is indeed the case. Finally TM1 has the option to turn on neo-classical effects (or curvature effects) and these can act stabilizing for the magnetic islands. Although not stated explicitly, perhaps some neo-classical effects were included to keep the island stable, whereas the simulations M3D-C1 do not include this effect.

6 Conclusions

The main goal of this research is to benchmark mode-penetration events in M3D-C1 so that they may be simulated in more realistic geometries, and to further understanding of mode-penetration events. To do so we expand on the available literature by adding novel components to the error-field penetration model, and by developing a set of visco-resistive equilibrium equations to initialize the simulations. We note the interesting discovery that localized forces near the magnetic island are found to have the effect of increasing the threshold error-field strength for which mode-penetration occurs, and thus might be used as an additional control parameter to ensure that the plasma does not become mode-penetrated.

After initializing M3D-C1 with the viso-resistive equilibrium equations in a manner resembling to the benchmark, we run the simulations to see if we find similar results. However, there are stark differences between benchmark case and the M3D-C1 case. Large quantitative and qualitative differences are found, and a mode-penetration like event is not observed.

This is seen in a number of different diagnostics. The island width is observed to be much larger in the M3D-C1 case as compared to the benchmark, and the island width does not become suppressed as in the benchmark case. The second diagnostic is the poloidal plasma velocity, which has a much lower magnitude than the benchmark case. It again does not show a mode-penetration event.

We suspect that the most likely culprit for this discrepancy is the inherent stability of the mode. In M3D-C1, the mode is inherently unstable, whereas in the benchmark case the mode is stable. This could be due to several reasons;

- slight differences in equilibrium profiles between benchmark and M3D-C1,
- different numerical methods for codes used in benchmark and M3D-C1,

- non-zero contributions of external driving forces near the magnetic island in the benchmark case, as compared to no contribution here in M3D-C1,
- possible inclusion of some neo-classical effects in the benchmark case, whereas these are not present in M3D-C1.
- The possible use of implicit sources to make the initial unperturbed equilibrium a solution to the time-dependent equation
- The possible use of a reduced MHD model in TM1

Besides these discrepancies, another interesting effect is found. Islands tend to migrate inwards during the simulations in M3D-C1. This can be explained as the combination of two effects; the current density profile tends to flatten in the magnetic island region, and the total amount of current is conserved. This in turn tends to drive down the current density on axis, and increase the safety factor on axis. Since the safety factor at the edge is constant (due to the fact that the plasma current is constant), one can conclude that the resonant surface drifts inwards.

Although the research goal has not been met yet, this work does show a clear way towards completing that goal, which will be expanded on in section 7. The main problem in running these simulations has been identified (mode stability). If solved we could set harder bounds on allowable error-field strengths in ITER, an important design constraint hopefully preventing fatal disruptive events.

7 Future recommendations

Finally, we make some recommendations for future directions of this research. We suggest that the benchmark case is initialized with the visco-resistive equilibrium profiles to check for stability. We also suggest that M3D-C1 is initialized with the profiles used in the benchmark case. This should point out if the discrepancy is a purely profile-dependent property, or if a more fundamental reason is the reason for this. If the stability issue is resolved, we suggest to run a set of different simulations, which mirror the benchmark case. It is expected that these simulations will need some tweaking to be numerically stable. When all simulations are converged, we'd suggest taking the most restrictive case (the simulation that needed the most tweaking by for example increasing hyper-diffusivity) and running all simulations again with these most restrictive settings. This should exclude effects which arise due to this nudging of input parameters.

If these new results obtained by M3D-C1 do follow the benchmark nicely, we suggest to run an extra set of simulations to ensure that this is indeed mode-penetration, and not a case without the bifurcation. One should take the analogue of the small-island benchmark case in M3D-C1 as a starting point (i.e. initialization) for new simulations. Using this as a starting point, one should run a host of simulations with increasing error-field strengths. If this is a true error-field penetration event, there should be a clear bifurcation in island width and plasma velocity where the critical field-strength is achieved. One could then do the same in reverse; take this mode-penetrated simulation as a starting point and decrease the field strength until some

threshold is crossed and the solution should jump back to a non mode-penetrated state. This bifurcating behaviour would be a clear indicator that we are observing a true mode-penetration event.

When these steps have been completed, an interesting step for future research would be to expand these simulations to full toroidal geometries with circular plasmas (in their poloidal cross-section). In this manner, we could take a small aspect-ratio limit and see if the results match the cylindrical cases. This would be completely novel. Finally, one could then run simulations which mirror experimental runs and compare the results.

Another peculiar discovery made during the research into the theory is that external driving forces near the magnetic island tend to drive the threshold field strength for which mode-penetration occurs upwards. This should be checked in currently available mode-penetration simulations, and in experiment. This is relevant as it might be used as an extra control parameter to ensure mode-penetration does not occur.

A Appendix

A.1 Fortran namelists

Here we showcase the namelists (or input files) used for the equilibrium code, and M3D-C1. Firstly, the equilibrium codes namelist is a s foillows:

```
! Numerical Options
! ==================
    drho        =   1E-5    ! Stepsize for forward Euler

! Model Options
! =============
    b_flat      =   0       ! Parameter indiciting if the
                            ! pressure will be calculated
                            ! consistently via the q profile
                            ! (b_flat = 1), or if one will
                            ! assume a flat b_z profile
                            ! (b_flat = 0). q-profile is
                            ! defined in the .f90 file
    eta_fac     =   10.0    ! Prefactor for spitzer resistivity
    mu_fac      =   1.0     ! Prefactor for viscosity, but also
                            ! for F0_real. This is to keep the
                            ! max velocity fixed.
! Physical parameters
! ===================
    ln_lambda   =   17.0    ! Plasma parameter
    z_ion       =   1       ! Charge number for ions
    beta        =   0.0     ! Fraction of non-Ohmic
                            ! heating (from an
                            ! external heat source)
    t_end       =   0.143   ! Fraction of central
                            ! temperature value at
                            ! edge
    p_inf       =   0.0122  ! Fraction of central
                            ! pressure value at
                            ! edge
    a           =   0.47    ! Minor radius
    R0          =   4.0     ! Major radius
    Ip          =   2.0E5   ! Plasma current
    kappa0      =   9.4E19  ! Heat diffusivity
    v_fin       =   0.0     ! Fraction of central
                            ! velocity value at
                            ! edge
    F0_real     =   1.05E0  ! Total toroidal force
                            ! density
    mu_v_real   =   1.57e-7 ! Viscosity
    q0          =   1.5     ! Central q0 value.
```

```
                              ! Only applicible iff
                              ! b_flat=0
```

The M3D-C1 namelist is as follows:

```
! I/O Options
! ===========
ntimemax = 20000 ! number of time steps
ntimepr = 50 ! number of time steps per output
iprint = 1 ! 1 = print detailed debug info
itimer = 1 ! 1 = print timing info

irestart = 1      ! 1 = read restart

iwrite_aux_vars = 1
iwrite_transport_coeffs = 1

ike_harmonics = 4
ibh_harmonics = 4

! iadapt = 1
! adapt_smooth = 0.02
!
! Numerical Method Options
! ========================
dt = 10.0 ! time step

integrator = 0 ! 0 = Crank-Nicholson, 1 = BDF2
thimp = 1.0 ! implicitness parameter for CN
imp_mod = 0
isplitstep = 1

int_pts_main = 12
int_pts_aux = 12
int_pts_diag = 12

ivform = 1
jadv = 1
isurface = 0

itime_independent = 0

regular = 1e-8

max_ke = 0.

! Model Options
! =============
itor = 0 ! 1 = toroidal geometry, 0 = slab geometry
```

```
linear = 0 ! 0 = nonlinear; 1 = linear
eqsubtract = 0 ! 1 = subtract equilibrium in nonlinear simulations
       numvar = 3 ! 1 = 2-field; 2 = 4-field; 3 = 6-field
       idens = 1 ! 1 = advance density
ipres = 0 ! 1 = include electron pressure equation
itemp = 1
ipressplit = 1
gyro = 0

inertia = 1

ion_mass = 1.
z_ion = 1.

tcur = 0.251503677612526
vloop = 5.276199467944493E-007
control_type = 1
control_p = -0.01
control_d =  0.
control_i = -1e-4

ibeam = 5
beam_rate = 2.0599973e+20
beam_x = 4.
beam_z = 0.
beam_v = 100000.000000000
beam_dr = 0.094


! Equilibrium Options
! ===================
       itaylor = 33 ! determines initial conditions
! 0: Tilting Cylinder
! 1: Taylor reconnection
! 2: Force-free Taylor state
! 3: GEM-reconnection
! 4: Wave propagation


iread_j = 1
iread_f = 1
iread_p = 1
iread_ne = 1
iread_omega = 1

xlim = 4.47
zlim = 0.0
```

```
rzero = 4.
p0 = 4e-2 ! total pressure
pi0 = 2e-2 ! ion pressure

irmp = 2
xzero = 4.
zzero = 0.
mpol = 2
eps = 1e-5 ! size of initial perturbation

! maxn = 20

ln = 1.0



! Transport Parameters
! ====================
iresfunc = 4
eta_fac = 10.0
eta_wall = 0.1
ivisfunc = 0
       amu = 4.303362378745227E-007 ! kinematic viscosity
amuc = 1.0e-4.
amupar = 0.
denm = 1.0e-8 ! density diffusion
kappat = 4.309514858657082E-007 ! isotropic thermal diffusion
kappar = 0.01 ! field-aligned thermal conductivity
ikapscale = 0

gam = 1.66666666666667 ! adiabatic constant

! db = 0.0322 ! ion skin depth

! hyper = 1e-10 ! tor cur dens hyper diff
! hyperi= 1e-10 ! pol cur dens hyper diff
! hyperc= 1e-10
! hyperv= 1e-10
hyperp =1e-9
imp_bf= 1 ! Implicit f equation
imp_hyper=1 ! Implicit for f
inocurrent_pol= 1 ! No poloidal current on boundary
iconst_n      = 0


! Boundary Conditions
! ===================
```

```
iconst_bz = 0
ifbound = 1

nonrect = 1

imulti_region = 1

mesh_filename = 'part.smb'
! mesh_filename = 'AnalyticModel.smb'
mesh_model = 'circle-0.02-0.0-0.0.txt'


xmag = 4. ! x-coordinate of magnetic axis
zmag = 0. ! z-coordinate of magnetic axis
pedge = 0.

ntor = 1

nplanes = 8
```

A.2 Scaling laws

From the visco-resistive equilibrium equations, we can derive a set of scaling laws which could be relevant for determining the sensitivity of certain parameters. From equations (2.93), (2.99) we know the scalings of T_0 p_0 and V_L on physical parameters. Using $n_0 \propto p_0/T_0$, we can also retrieve a scaling law for density. With density handy, all timescales can easily be found. All relevant scaling laws are found to be

$$
\begin{aligned}
&T_0 \propto \frac{\eta_0^{2/5} I_p^{4/5}}{a^{4/5} \kappa_0^{2/5}}, \qquad && p_0 \propto \frac{I_p^2}{a^2}, \qquad && n_0 \propto \frac{I_p^{6/5} \kappa_0^{2/5}}{a^{6/5} \eta_0^{2/5}}, \\
&B_\phi \propto \frac{I_p R_0}{a^2}, && \tau_A \propto \frac{a^{7/5} \kappa_0^{1/5}}{\eta_0^{1/5} I_p^{2/5}}, && \tau_R \propto \frac{a^{4/5} I_p^{6/5}}{\eta_0^{2/5} \kappa_0^{3/5}}, \\
&\tau_V \propto \frac{a^{4/5} I_p^{6/5} \kappa_0^{2/5}}{\eta_0^{2/5} \text{מ}_0}, && S \propto \frac{I_p^{8/5}}{a^{3/5} \eta_0^{1/5} \kappa_0^{4/5}}, && P_m \propto \frac{\text{מ}_0}{\kappa_0}.
\end{aligned}
\tag{A.1}
$$

A.3 Building a python-friendly plotting environment

To make plotting easier (and more importantly, to circumvent using IDL), we have build an object oriented python plotting environment. The object has the following structure:

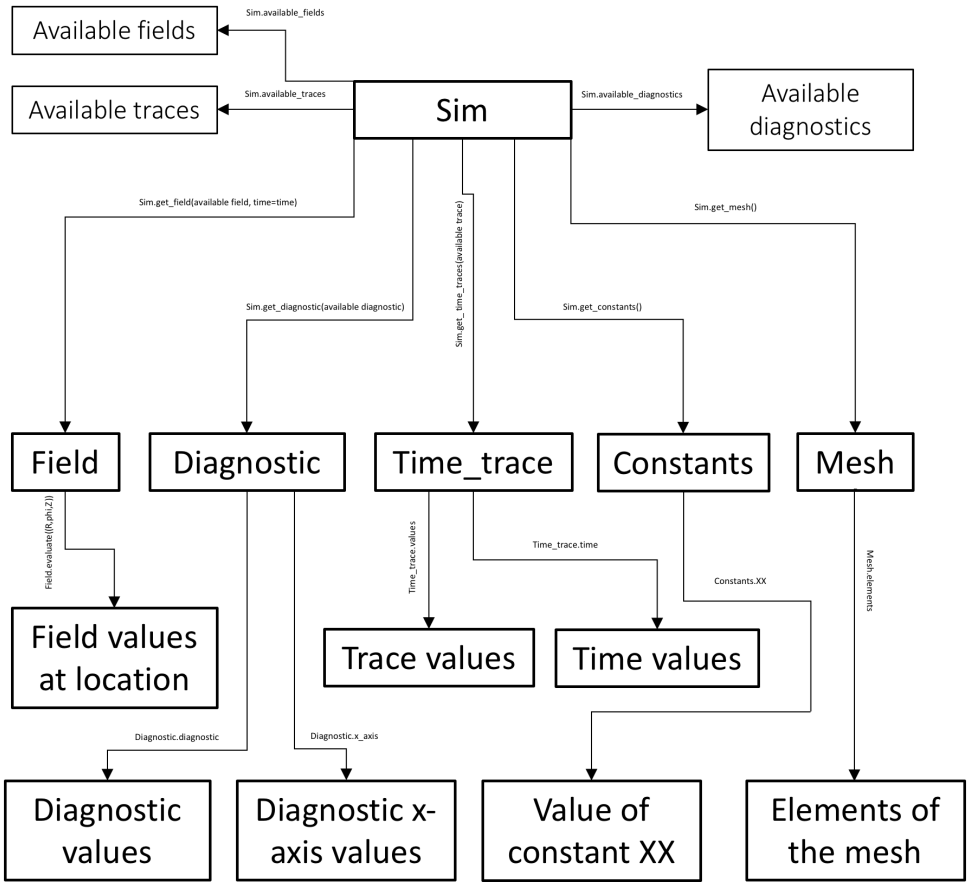

Figure A.1: The main simulation object with all of its subclasses. The available fields, time traces, and diagnostics can all be accessed within the object. The constants can by found by checking all the attributes of "Constants". The lines indicate the commands that have to be used, and the blocks indicate the objects.

Using this structure, plotting routines can be build easily and without much code. Most of the IDL routines have been reproduced in python so that people fimiliar with IDL have an easy time transferring. The python plotting routines, and a manual for using them, have been added to the M3D-C1 github repository.

A.4 Methodology for field-line tracing

We monitor the island width in all the simulations. This is done by solving the field-line tracing equation for the magnetic fields (giving us magnetic field lines). Given a magnetic field $\mathbf{B}$ at time t_0, the field line (parameterized as $\mathbf{x}(\lambda)$) obeys the following differential equation:

$$\frac{\partial \mathbf{x}(\lambda)}{\partial \lambda} = \mathbf{B}(\mathbf{x}(\lambda), t_0). \tag{A.2}$$

This equation can be discretized and solved numerically in the following way,

$$\begin{aligned} \Delta\mathbf{x} &= \mathbf{B}(\mathbf{x}_i, t_0)\Delta\lambda, \\ \mathbf{x}_{i+1} &= \mathbf{x}_i + \Delta\mathbf{x}. \end{aligned} \tag{A.3}$$

The true field-line tracing routine uses a more complex integrating routine with smaller accumulative errors, but the essence is the same. Solving this equation for different initial conditions (encapsulated in its initial position $\mathbf{x}_0$), we find a set of magnetic field lines. Finally, we make a Poincaré plot of these magnetic field lines by plotting where the field lines intersect a given toroidal cross-section. This leaves us with a set of intersection coordinates per field line. An exemplary Poincaré plot is provided in figure A.2.

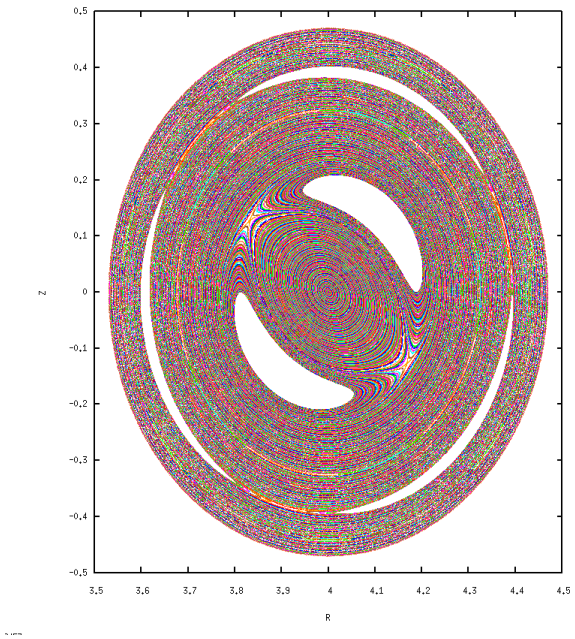

Figure A.2: Exemplary Poincaré plot. The neighboring points of the same color are from the same field-line. A clear magnetic-island structure can be seen, with both a $(2, 1)$ and a $(3, 1)$ island chain.

From these Poincaré plots, the island width is extracted in the following fashion. Firstly all the points are converted from (R, Z) coordinates to cylindrical coordinates

(i.e. (r, θ)), with the magnetic axis (the central magnetic field line) as the origin. Ordering the coordinates in θ (the cylindrical angle coordinate), we get a list of consecutive (meaning consecutive in the poloidal angle) radial coordinates. Per field line we take the difference between consecutive radial coordinates, and save only the largest one per field line. We then take the largest difference for all field lines to be the island width. When sampling is dense enough, this definition of island width is equivalent to the following. The island width is the largest difference in the radial coordinate for fixed a fixed poloidal angle.

A.5 Analytical model for the Kadomtsev sawtooth process

We note some other work, which has been done in conjunction with Chris Smiets (a fellow colleague at the lab). We expected that it was possible to build a straightforward analytical model for a Kadomtsev sawtooth process, which captured the essentials (reconnection of magnetic field lines, the replacement of the magnetic axis by a new one, the changes of the q profile). The magnetic field is described by $\mathbf{B} = \nabla \times (\psi\hat{\phi})$. Please note that we do include curvature effects in this model (i.e., we are using true toroidal coordinates) We postulate that only three functions were needed to fully describe the essentials,

ψ_0 = the initial equilibrium magnetic field with $q_0 < 1$,
ψ_∞ = the equilibrium magnetic field after reconnection has occurred,
ψ_{mode} = a function with a $(m = 1, n = 1)$ mode structure.

The final profile ψ_∞ can be calculated from the initial profile ψ_0, as is shown in [27]. Note that there is no reference to time-scales in this model. We combine and parameterize the functions in the following fashion:

$$\psi(\alpha, \epsilon) = (1 - \epsilon)\psi_0 + \epsilon\psi_\infty + \alpha\psi_{mode} \tag{A.4}$$

We choose the following path in the parameter space (α, ϵ):

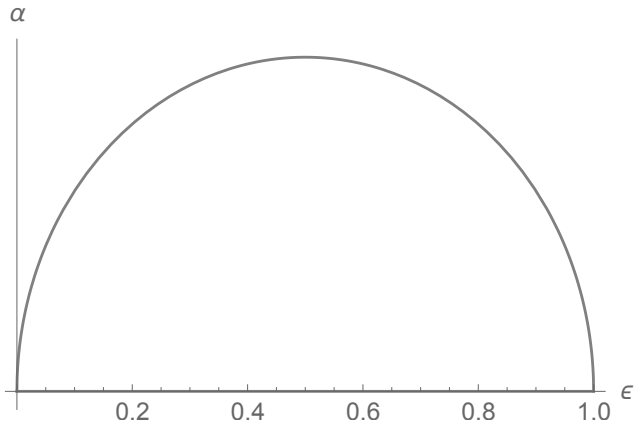

Figure A.3: Path in parameter space. α rises up to some maximum value α_{max}, and ϵ is bounded between 0 and 1. The path is followed in a clockwise manner.

Using this path in parameter space, we employ a field-line tracing code to investigate the structure of the magnetic field in a Poincaré plot. The results can be seen in figure A.4. A more in depth treatment of the methodology and results is currently being written.

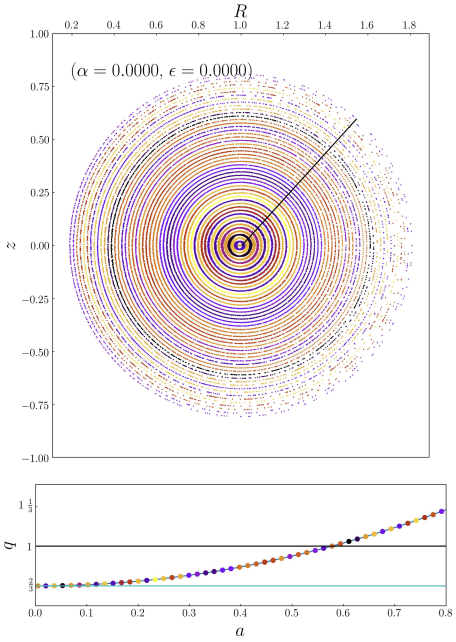

(a) Poincare plot at $(\alpha = 0.0, \epsilon = 0.0)$

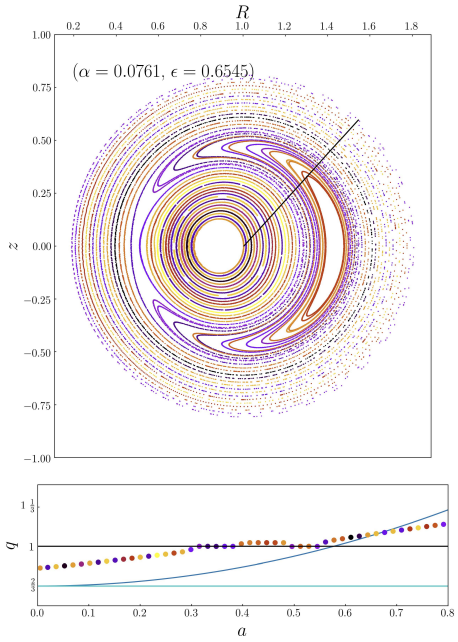

(b) Poincare plot at $(\alpha = 0.08, \epsilon = 0.7)$

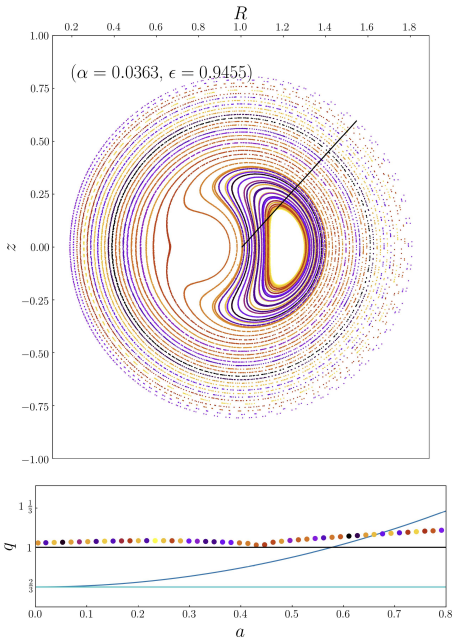

(c) Poincare plot at $(\alpha = 0.03, \epsilon = 0.9)$

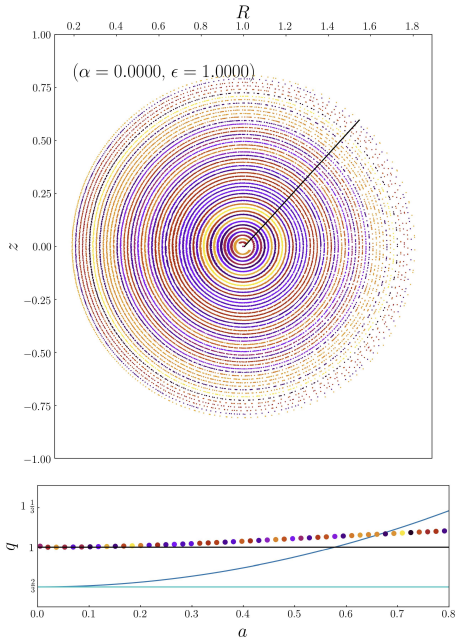

(d) Poincare plot at $(\alpha = 0, \epsilon = 1.0)$

Figure A.4: Poincare plots as one traverses parameter space.

References

[1] J. A. Curry, J. L. Schramm, and E. E. Ebert, "Sea ice-albedo climate feedback mechanism," *Journal of Climate*, vol. 8, no. 2, pp. 240–247, 1995.

[2] A. A. Bloom, P. I. Palmer, A. Fraser, D. S. Reay, and C. Frankenberg, "Large-scale controls of methanogenesis inferred from methane and gravity spaceborne data," *Science*, vol. 327, no. 5963, pp. 322–325, 2010.

[3] J. W. Milnor and D. W. Weaver, *Topology from the differentiable viewpoint*. Princeton university press, 1997.

[4] J. Lawson, "Some criteria for a power producing thermonuclear reactor," *Proceedings of the Physical Society. Section B*, vol. 70, no. 1, pp. 6–10, 1957.

[5] Eurofusion, "Tokamak principle," 2005. [Online]. Available: https://www.euro-fusion.org/news/detail/detail/News/tokamak-principle/

[6] P. C. de Vries, M. F. Johnson, B. Alper, P. Buratti, T. C. Hender, H. R. Koslowski, and V. Riccardo, "Survey of disruption causes at JET," *Nuclear Fusion*, vol. 51, no. 5, p. 53018, 2011. [Online]. Available: http://dx.doi.org/10.1088/0029-5515/51/5/053018

[7] R. Fitzpatrick and T. C. Hender, "The interaction of resonant magnetic perturbations with rotating plasmas," *Physics of Fluids B: Plasma Physics*, vol. 3, no. 3, pp. 644–673, 1991.

[8] H. R. Koslowski, Y. Liang, A. Krämer-Flecken, K. Löwenbrück, M. von Hellermann, E. Westerhof, R. C. Wolf, O. Zimmermann, and T. team, "Dependence of the threshold for perturbation field generated m/n= 2/1 tearing modes on the plasma fluid rotation," *Nuclear Fusion*, vol. 46, no. 8, p. L1, 2006.

[9] R. J. Buttery, M. De'Benedetti, T. C. Hender, and B. J. D. Tubbing, "Error field experiments in JET," *Nuclear fusion*, vol. 40, no. 4, p. 807, 2000.

[10] S. M. Wolfe, I. H. Hutchinson, R. S. Granetz, J. Rice, A. Hubbard, A. Lynn, P. Phillips, T. C. Hender, D. F. Howell, and R. J. La Haye, "Non-axisymmetric field effects on Alcator C-Mod," *Physics of plasmas*, vol. 12, no. 5, p. 56110, 2005.

[11] R. C. Wolf, W. Biel, M. F. M. De Bock, K. H. Finken, S. Günter, G. M. D. Hogeweij, S. Jachmich, M. W. Jakubowski, R. J. E. Jaspers, and A. Krämer-Flecken, "Effect of the dynamic ergodic divertor in the TEXTOR tokamak on MHD stability, plasma rotation and transport," *Nuclear fusion*, vol. 45, no. 12, p. 1700, 2005.

[12] R. J. Buttery, M. D. Benedetti, D. A. Gates, Y. Gribov, T. C. Hender, R. J. L. Haye, P. Leahy, J. A. Leuer, A. W. Morris, A. Santagiustina, J. T. Scoville, B. J. D. Tubbing, J. E. T. Team, C.-D. R. Team, and D.-D. Team, "Error field mode studies on JET, COMPASS-D and DIII-D, and implications for ITER," *Nuclear Fusion*, vol. 39, no. 11Y, pp. 1827–1835, 1999. [Online]. Available: http://dx.doi.org/10.1088/0029-5515/39/11Y/323

[13] M. T. Beidler, J. D. Callen, C. C. Hegna, and C. R. Sovinec, "Nonlinear modeling of forced magnetic reconnection in slab geometry with NIMROD," *Physics of Plasmas*, vol. 24, no. 5, p. 52508, 2017. [Online]. Available: https://doi.org/10.1063/1.4982814

[14] ——, "Mode penetration induced by transient magnetic perturbations," *Physics of Plasmas*, vol. 25, no. 8, p. 82507, 2018.

[15] R. Fitzpatrick, "Interaction of tearing modes with external structures in cylindrical geometry (plasma)," *Nuclear Fusion*, vol. 33, no. 7, pp. 1049–1084, 1993.

[16] Q. Yu, S. Günter, Y. Kikuchi, and K. H. Finken, "Numerical modelling of error field penetration," *Nuclear Fusion*, vol. 48, no. 2, p. 24007, 2008. [Online]. Available: http://dx.doi.org/10.1088/0029-5515/48/2/024007

[17] A. Cole and R. Fitzpatrick, "Drift-magnetohydrodynamical model of error-field penetration in tokamak plasmas," *Physics of Plasmas*, vol. 13, no. 3, p. 32503, 3 2006. [Online]. Available: https://doi.org/10.1063/1.2178167

[18] F. Militello and F. L. Waelbroeck, "Error field penetration in the presence of diamagnetic effects," *Nuclear Fusion*, vol. 49, no. 6, p. 65018, 5 2009. [Online]. Available: https://doi.org/10.1088%2F0029-5515%2F49%2F6%2F065018

[19] J. P. Freidberg, "Ideal magnetohydrodynamics," 1987.

[20] S. I. Braginskii, "Transport processes in a plasma," *Reviews of plasma physics*, vol. 1, 1965.

[21] I. P. Shkarofsky, T. W. Johnston, M. P. Bachynski, and J. L. Hirshfield, "The particle kinetics of plasmas," *American Journal of Physics*, vol. 35, pp. 551–552, 1967.

[22] N. M. Ferraro and S. C. Jardin, "Calculations of two-fluid magnetohydrodynamic axisymmetric steady-states," *Journal of Computational Physics*, 2009.

[23] C. K. Batchelor and G. K. Batchelor, *An introduction to fluid dynamics*. Cambridge university press, 2000.

[24] R. Fitzpatrick and T. C. Hender, "The interaction of resonant magnetic perturbations with rotating plasmas," *Physics of Fluids B*, vol. 3, no. 3, pp. 644–673, 1991.

[25] A. B. Mikhailovskii, S. V. Konovalov, V. D. Pustovitov, and V. S. Tsypin, "An approach to calculation of magnetic island rotation frequency," *Physics of Plasmas*, vol. 7, no. 6, pp. 2530–2538, 2000.

[26] P. H. Rutherford, "Nonlinear growth of the tearing mode," *Physics of Fluids*, vol. 16, no. 11, pp. 1903–1908, 11 1973. [Online]. Available: https://aip.scitation.org/doi/abs/10.1063/1.1694232

[27] D. Biskamp, *Nonlinear magnetohydrodynamics*. Cambridge University Press, 1997, vol. 1.

[28] G. Ara, B. Basu, B. Coppi, G. Laval, M. N. Rosenbluth, and B. V. Waddell, "Magnetic reconnection and m = 1 oscillations in current carrying plasmas," *Annals of Physics*, 1978.

[29] R. Mackenbach, "Visco-resistive cylindrical equilibrium profiles," 2019. [Online]. Available: https://github.com/RalfMackenbach/Ohmic-Equilbrium.git

[30] O. Neubauer, G. Czymek, B. Giesen, P. W. Hüttemann, M. Sauer, W. Schalt, and J. Schruff, "Design Features of the Tokamak TEXTOR," *Fusion Science and Technology*, vol. 47, no. 2, pp. 76–86, 2005. [Online]. Available: https://doi.org/10.13182/FST05-A689

[31] R. Jaspers, K. H. Finken, G. Mank, F. Hoenen, J. A. Boedo, N. J. L. Cardozo, and F. C. Schuller, "Experimental investigation of runaway electron generation in TEXTOR," *Nuclear fusion*, vol. 33, no. 12, p. 1775, 1993.

[32] K. H. Finken, S. S. Abdullaev, M. F. M. de Bock, M. von Hellermann, M. Jakubowski, R. Jaspers, H. R. Koslowski, A. Krämer-Flecken, M. Lehnen, Y. Liang, A. Nicolai, R. C. Wolf, O. Zimmermann, M. de Baar, G. Bertschinger, W. Biel, S. Brezinsek, C. Busch, A. J. H. Donné, H. G. Esser, E. Farshi, H. Gerhauser, B. Giesen, D. Harting, J. A. Hoekzema, G. M. D. Hogeweij, P. W. Hüttemann, S. Jachmich, K. Jakubowska, D. Kalupin, F. Kelly, Y. Kikuchi, A. Kirschner, R. Koch, M. Korten, A. Kreter, J. Krom, U. Kruezi, A. Lazaros, A. Litnovsky, X. Loozen, N. J. Lopes Cardozo, A. Lyssoivan, O. Marchuk, G. Matsunaga, P. Mertens, A. Messiaen, O. Neubauer, N. Noda, V. Philipps, A. Pospieszczyk, D. Reiser, D. Reiter, A. L. Rogister, M. Sakamoto, A. Savtchkov, U. Samm, O. Schmitz, R. P. Schorn, B. Schweer, F. C. Schüller, G. Sergienko, K. H. Spatschek, G. Telesca, M. Tokar, R. Uhlemann, B. Unterberg, G. Van Oost, T. Van Rompuy, G. Van Wassenhove, E. Westerhof, R. Weynants, S. Wiesen, and Y. H. Xu, "Toroidal Plasma Rotation Induced by the Dynamic Ergodic Divertor in the TEXTOR Tokamak," *Physical Review Letters*, vol. 94, no. 1, p. 15003, 1 2005. [Online]. Available: https://link.aps.org/doi/10.1103/PhysRevLett.94.015003

[33] S. C. Jardin, "A triangular finite element with first-derivative continuity applied to fusion MHD applications," *Journal of Computational Physics*, vol. 200, no. 1, pp. 133–152, 2004. [Online]. Available: http://www.sciencedirect.com/science/article/pii/S0021999104001366

[34] S. C. Jardin, N. Ferraro, X. Luo, J. Chen, J. Breslau, K. E. Jansen, and M. S. Shephard, "The M3D-C1approach to simulating 3D 2-fluid magnetohydrodynamics in magnetic fusion experiments," *Journal of Physics: Conference Series*, vol. 125, p. 12044, 7 2008. [Online]. Available: https://doi.org/10.1088%2F1742-6596%2F125%2F1%2F012044

[35] N. M. Ferraro, S. C. Jardin, L. L. Lao, M. S. Shephard, and F. Zhang, "Multi-region approach to free-boundary three-dimensional tokamak equilibria and resistive wall instabilities," *Physics of Plasmas*, vol. 23, no. 5, p. 56114, 2016.